ANNUAL REVIEWS

Annual Review of Astronomy and Astrophysics

Circumbinary Accretion: From Binary Stars to Massive Binary Black Holes

Dong Lai[1] and Diego J. Muñoz[2,3,4]

[1]Department of Astronomy, Center for Astrophysics and Planetary Science, Cornell University, Ithaca, New York, USA; email: dong@astro.cornell.edu

[2]Center for Interdisciplinary Exploration and Research in Astrophysics, Department of Physics & Astronomy, Northwestern University, Evanston, Illinois, USA

[3]Facultad de Ingeniería y Ciencias, Universidad Adolfo Ibáñez, Peñalolén, Santiago, Chile

[4]Millennium Institute for Astrophysics, Chile

Annu. Rev. Astron. Astrophys. 2023. 61:517–60

First published as a Review in Advance on June 20, 2023

The *Annual Review of Astronomy and Astrophysics* is online at astro.annualreviews.org

https://doi.org/10.1146/annurev-astro-052622-022933

Keywords

stars, binaries, star formation, black hole physics, supermassive black holes, accretion disks, protoplanetary disks, exoplanets, hydrodynamics

Abstract

We review recent works on the dynamics of circumbinary accretion, including time variability, angular momentum transfer between the disk and the binary, and the secular evolution of accreting binaries. These dynamics impact stellar binary formation/evolution, circumbinary planet formation/migration, and the evolution of (super)massive black hole binaries. We discuss the dynamics and evolution of inclined/warped circumbinary disks and connect with observations of protoplanetary disks. A special kind of circumbinary accretion involves binaries embedded in big disks, which may contribute to the mergers of stellar-mass black holes in AGN disks. Highlights include the following:

- Circumbinary accretion is highly variable, being modulated at P_b (the binary period) or $\sim 5P_b$, depending on the binary eccentricity e_b and mass ratio q_b.
- The inner region of the circumbinary disk can develop coherent eccentric structure, which may modulate the accretion and affect the physical processes (e.g., planet migration) taking place in the disk.

- Over long timescales, circumbinary accretion steers binaries toward equal masses, and it does not always lead to binary orbital decay. The secular orbital evolution depends on the binary parameters (e_b and q_b) and on the thermodynamic properties of the accreting gas.
- A misaligned disk around a low-eccentricity binary tends to evolve toward coplanarity due to viscous dissipation. But when e_b is significant, the disk can evolve toward "polar alignment," with the disk plane perpendicular to the binary plane.

Contents

1. INTRODUCTION

Circumbinary disk (CBD) accretion plays an important role in the evolution of many types of astrophysical systems, ranging from young binary stars, main sequence, and post–main sequence binaries to supermassive binary black holes (SMBHs). **Figure 1** illustrates the basic features of such accretion: Gas from large distances gradually spirals toward the binary in a CBD driven by viscous dissipation; the disk is truncated at a few binary separations by the varying gravitational force from the binary (the "egg beater"), forming a cavity; the gas at the inner edge falls inward through accretion streams toward individual stars [or black holes (BHs)], forming circumsingle disks (CSDs, or "mini-disks") and eventually accreting onto each star.

Circumbinary accretion has long been suggested to exist around binary massive black holes (MBHs) following galaxy mergers (e.g., Begelman et al. 1980, Milosavljević & Merritt 2001, Escala et al. 2005, Milosavljević & Phinney 2005, Dotti et al. 2007, Cuadra et al. 2009, Chapon et al. 2013). This has been demonstrated in many numerical simulations over the years. An example is provided

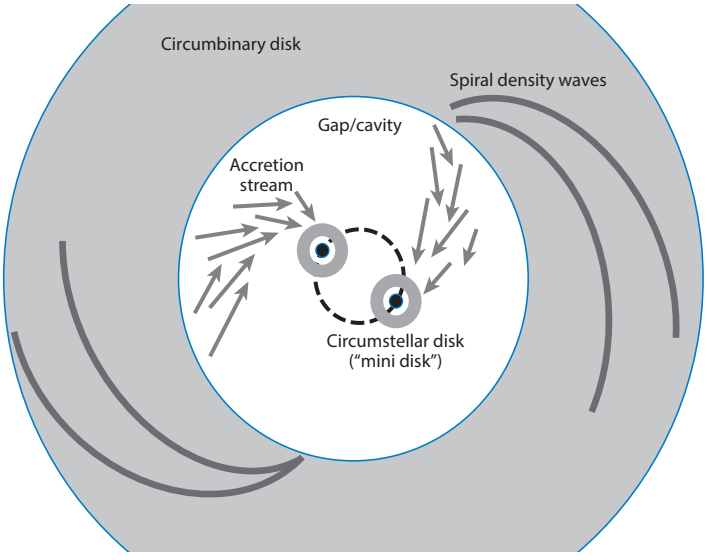

Figure 1

An illustration of the basic features of circumbinary accretion. Illustration created by Ryan Miranda (2017).

by Mayer et al. (2007): two galaxies (each containing an MBH), initially separated at ∼100 kpc, collide with each other and eventually end up as two MBHs separated by ∼10 pc and surrounded by an extended (∼100 pc) disk/torus at the center of the merged galaxy.

Some of the key questions concerning circumbinary accretion are, Does the binary lose or gain angular momentum and how does the binary orbit evolve? The first discussion of this issue appeared in Begelman et al. (1980):

> . . .infall of gas onto the binary can also lead to some orbital evolution. Gas may be flung out of the system, acquiring energy (and angular momentum) at the expense of the binary; alternatively, gas may accrete onto the larger hole, causing orbital contraction as the product Mr is adiabatically invariant. In either case, the evolution timescale is

$$t_{\rm gas} \sim 10^8 M_8 \left(\dot{M}/1\ {\rm M}_\odot\ {\rm year}^{-1}\right)^{-1}\ {\rm year}.$$

As we discuss in this review (see Section 3), this issue has been controversial and the prevailing view has been challenged by recent studies. The evolution of SMBH binaries undergoing gas accretion may directly impact the low-frequency gravitational wave (GW) signatures probed by space interferometers such as *Laser Interferometer Space Antenna* (LISA; Amaro-Seoane et al. 2017) and pulsar timing arrays (Burke-Spolaor et al. 2019; see Section 4.1).

Circumbinary accretion disks are a natural byproduct of binary star formation via disk fragmentation (e.g., Bonnell & Bate 1994, Kratter et al. 2008, Offner et al. 2022). A number of these disks have been observed around Class I/II young stellar binaries—well-known examples include GG Tau, DQ Tau, and UZ Tau E (e.g., Dutrey et al. 1994, Mathieu et al. 1997, Phuong et al. 2020)—and recently even around much younger Class 0 objects like L1448 IRS3B (Tobin et al. 2016) and IRAS 16293-2422 A (Maureira et al. 2020). With Atacama Large Millimeter/submillimeter Array (ALMA), many CBDs have been discovered through direct imaging (e.g., Czekala et al. 2021). Recent observations have revealed that the disk can be highly misaligned with the central binary (Kennedy et al. 2019)—an issue we address in Section 5. The observed properties of "mature"

stellar binaries (such as the mass ratio distribution) may have been shaped by circumbinary accretion at the earlier (protostellar) phase (see Section 4.2).

Circumbinary disks have also been found around many post-AGN binaries (e.g., Van Winckel 2018). These "second-generation" disks, likely formed as a result of binary interactions during the asymptotic giant branch (AGB) phase, can impact the evolution of the systems (see Section 4.4).

Starting from NASA's Kepler mission, planets have been found around stellar binaries using the transit method (e.g., Doyle et al. 2011). So far, more than a dozen of such systems are known (see Welsh & Orosz 2018, Kostov et al. 2020, and references therein). An interesting feature of these circumbinary systems is that many of the planets are found very close (within a factor of 1.5) to the stability limit, i.e., if the semimajor axis of the planet is a bit smaller (e.g., by 10% in the case of Kepler-16b), the planet would be ejected from the system. These planets are unlikely to have formed in situ but must have migrated from far away in the protoplanetary disk. The dynamics of CBDs can strongly influence the formation and migration of the planets (see Section 4.3).

Recently, a special type of circumbinary accretion has gained interest, in connection with the GW sources detected by LIGO (Laser Interferometer Gravitation-Wave Observatory)/Virgo. It has been suggested that merging stellar BH binaries can be produced in AGN disks (e.g., Bartos et al. 2017, Stone et al. 2017, McKernan et al. 2018, Tagawa et al. 2020). The hydrodynamical flows generated by binaries embedded in AGN disks have several distinct features compared to normal circumbinary accretion disks (see Section 6).

2. THEORY AND SIMULATION OF CIRCUMBINARY DISK ACCRETION: BASIC CONCEPTS AND OVERVIEW

We first review some of the key theoretical concepts related to circumbinary accretion. The analytic aspect of binary–disk interaction through gravitational forcing is relatively straightforward, at least in the linear regime (i.e., when the perturbation of the disk by the binary is weak). The gravitational potential produced by the binary (with total mass $M_{\rm b}$, semimajor axis $a_{\rm b}$, and eccentricity $e_{\rm b}$) on the disk (assumed to be aligned with the binary plane) at the position $\mathbf{r} = (r, \phi)$ (measured from the binary's center of mass) can be written as (Goldreich & Tremaine 1980)

$$\Phi(\mathbf{r}, t) = \sum_{m=0}^{\infty} \sum_{n=-\infty}^{\infty} \Phi_{mn}(r) \cos\left[m\phi - (m\Omega_{\rm b} + n\kappa_{\rm b})t\right], \tag{1.}$$

where $\Omega_{\rm b} = (GM_{\rm b}/a_{\rm b}^3)^{1/2}$ is the mean angular frequency (or mean motion) of the binary, and $\kappa_{\rm b}$ is the radial epicyclic frequency. For binaries in Keplerian orbits, $\kappa_{\rm b} = \Omega_{\rm b}$. The potential component Φ_{mn} depends on $e_{\rm b}$ and $a_{\rm b}/r$; to the leading order in $e_{\rm b}$, we have $\Phi_{mn} \sim e_{\rm b}^{|n|}\Phi_{mm}$. For $m > 0$, the (mn)-potential rotates with the pattern frequency

$$\omega_{mn} = \frac{m\Omega_{\rm b} + n\kappa_{\rm b}}{m} = \frac{N\Omega_{\rm b}}{m}, \tag{2.}$$

(where $N = m + n$ and the second equality assumes $\kappa_{\rm b} = \Omega_{\rm b}$), and excites spiral density waves at the Lindblad resonances (LRs), where

$$\omega_{\rm mn} - \Omega(r) = \pm\frac{\kappa(r)}{m}, \tag{3.}$$

with the plus (minus) symbol corresponding to the outer (inner) LR. As the CBD is approximately Keplerian, $\kappa \simeq \Omega \simeq (GM_{\rm b}/r^3)^{1/2}$, the LRs are located at

$$\frac{\Omega\,(r_{\rm LR})}{\Omega_{\rm b}} \simeq \frac{N}{m \pm 1} \quad \text{or} \quad \frac{r_{\rm LR}}{a_{\rm b}} \simeq \left(\frac{m \pm 1}{N}\right)^{2/3}. \tag{4.}$$

The torque on the disk at an LR is (Goldreich & Tremaine 1979)

$$T_{mn}^{\rm LR} = -m\pi^2 \left[\Sigma \left(\frac{{\rm d}D}{{\rm d}\ln r} \right)^{-1} |\Psi_{mn}|^2 \right]_{r_{\rm LR}}, \quad 5.$$

where Σ is the disk surface density, $D = \kappa^2 - m^2(\Omega - \omega_{mn})^2$, and

$$\Psi_{mn} = \frac{{\rm d}\Phi_{mn}}{{\rm d}\ln r} + \frac{2\Omega}{\Omega - \omega_{\rm mn}} \Phi_{mn}. \quad 6.$$

At the outer LRs (OLRs; which are most relevant for CBDs), $({\rm d}D/{\rm d}\ln r) = -3N^2\Omega_{\rm b}^2/(m+1)$, we find $T_{mn}^{\rm OLR} > 0$, i.e., the disk particles gain angular momentum from the binary through resonant gravitational torques. This is a general result: A rotating potential always transports angular momentum from higher to lower angular velocity (Lynden-Bell & Kalnajs 1972, Goldreich & Sari 2003). The associated energy transfer rate to the disk through the LR is given by

$$\frac{{\rm d}E_{\rm d}}{{\rm d}t} = \omega_{mn} \frac{{\rm d}J_{\rm d}}{{\rm d}t} = \omega_{mn} T_{mn}^{\rm LR}. \quad 7.$$

These expressions are useful for determining how gravitational binary-disk interaction affects the binary orbit (see Section 4.4).

However, the disk particles lose angular momentum through viscous torque. Assuming the α-ansatz for the kinematic viscosity coefficient, $\nu = \alpha c_{\rm s}^2/\Omega$ (where $c_{\rm s}$ is the disk sound speed), the viscous torque is given by (e.g., Pringle 1981)

$$T_\nu = 3\pi\nu\Sigma\Omega r^2 = 3\pi\alpha h^2 \Sigma\Omega^2 r^4, \quad 8.$$

where $h = H/r$ is the disk aspect ratio. A gap is opened at the (mn)-LR if $T_{mn} \geq T_\nu$ (Artymowicz & Lubow 1994). In this picture, the radius $r_{\rm cav}$ of the inner cavity of a CBD is determined by the largest radius at which a gap can be cleared.

As an example, for a circular binary, the dominant potential has $m = 2$ and $n = 0$, with $\Phi_{mn} \simeq -3G\mu_b a_{\rm b}^2/(4r^3)$ (assuming $r \gg a_{\rm b}$, where $\mu_{\rm b}$ is the reduced mass of the binary). The OLR is located at $r_{\rm LR} \simeq (3/2)^{2/3} a_{\rm b}$, and the LR torque is $T_{20}^{\rm LR} \simeq (49\pi^2/2)\Sigma(\Phi_{20}/\Omega_{\rm b})^2$. Gap opening at the OLR requires $T_{20}^{\rm LR} \gtrsim T_\nu$, i.e.,

$$\alpha h^2 \lesssim 0.14 \left(\frac{4\mu_{\rm b}}{M_{\rm b}} \right)^2, \quad 9.$$

which is a condition easily satisfied for binaries with comparable component masses. For a small but finite $e_{\rm b}$, the gap is cleared by the $m = 2$ and $n = -1$ potential (with $\Phi_{mn} \propto e_{\rm b}$), and the corresponding OLR is at $r_{\rm LR} \simeq 3^{2/3} a_{\rm b}$.

Miranda & Lai (2015) considered eccentric binaries with general mass ratios and binary–disk inclination angles. For typical disk $c_{\rm s}$ and viscosity parameter, the inner radius $r_{\rm cav}$ of the CBD is found to be (2–3)$a_{\rm b}$ and depends on $e_{\rm b}$ in a discrete manner. Misaligned disks generally have smaller inner radii than aligned disks. In any case, it is important to recognize that such theoretical calculation of the inner disk radius has obvious limitations, as real disks are expected to have a fuzzy and dynamical inner boundary, with gas streaming into the cavity. Numerical simulations are needed to capture the whole complexities of binary–disk interactions, especially near the inner truncation radius.

More subtle resonant binary–disk interactions can also play a role in the dynamics of CBDs, such as the parametric instability associated with Lindblad resonances (see Section 3.3) that can excite disk eccentricity (Hirose & Osaki 1990; Lubow 1991a,b). In addition, for an eccentric binary, secular (orbital-averaged) interaction may affect the disk eccentricity evolution (Miranda et al. 2017, Lubow 2022; see Section 3.3)

Because of the importance of circumbinary accretion in various astrophysical contexts, many numerical simulations have been carried out over the years. Some works were based on smoothed particle hydrodynamics (SPH; e.g., Bate et al. 1995, Artymowicz & Lubow 1996, Escala et al. 2005, Cuadra et al. 2009, Roedig et al. 2012, Pelupessy & Portegies Zwart 2013, Ragusa et al. 2016). Others used grid-based Eulerian hydrodynamical methods: These include, among others, Günther & Kley (2002; hybrid grid), MacFadyen & Milosavljević (2008; `FLASH`, polar grid with inner cavity excised), Hanawa et al. (2010; nested cartesian grid), de Val-Borro et al. (2011; cartesian grid), D'Orazio et al. (2013; `FLASH`, polar grid with inner cavity excised), Lines et al. (2015; `FARGO`, polar grid with inner cavity excised), and Miranda et al. (2017; `PLUTO`, polar grid with inner cavity excised). Most simulations solved hydrodynamical equations with parameterized viscosity, but some short-duration (essentially) Newtonian magnetohydrodynamic (MHD) simulations have also been carried out (Noble et al. 2012, Shi et al. 2012, Shi & Krolik 2015, Bowen et al. 2019) and even general relativistic magnetohydrodynamic (GRMHD) simulations, in which a time-dependent, sewn-together metric (e.g., Matzner et al. 1998) can be prescribed in order to take into account the Kerr metric in the vicinity of each BH (Combi et al. 2021, 2022).

Numerical simulations of circumbinary accretion are challenging because of the wide spatial range involved and the multiple timescales on which variability takes place (**Figure 2**). The accreting gas flows from a large, viscously evolving disk surrounding the binary and transitions into plunging accretion streams, which then feed the CSDs around each individual binary component, which accretes mass at spatial scales typically much smaller than the binary separation. In addition, because the flow in the disk and near the binary is highly dynamical, determining the long-term effect of the flow on the binary requires sufficiently long simulations with careful averaging carried out.

In recent years, several finite-volume moving mesh codes have been used to study circumbinary accretion. The first is `DISCO`, which utilizes a moving ring grid (Farris et al. 2014, D'Orazio et al. 2016, Tang et al. 2017, Duffell et al. 2020). Another is `AREPO` (Muñoz & Lai 2016; Muñoz et al. 2019, 2020). The general-purpose grid-based Gudunov code `ATHENA++` has also been used for long-term simulations of CBDs (Moody et al. 2019; Wang et al. 2022a,b).

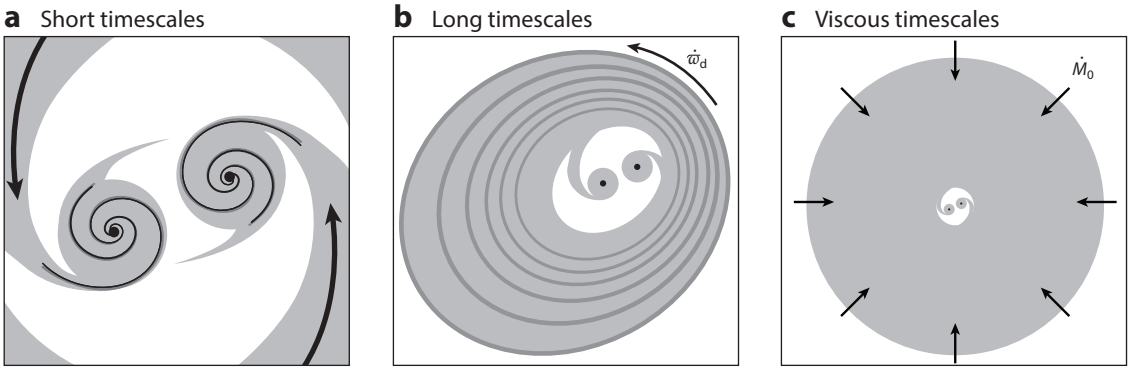

Figure 2

Some relevant timescales involved in circumbinary accretion. (*a*) Dynamical timescales: Variability is measured in the accretion rate on timescales on the order of the binary orbital period. (*b*) Secular timescales: Variability is measured in the accretion rate on timescales of hundreds of binary orbital periods in tandem with the secular apsidal precession of the inner disk. (*c*) Viscous timescales: For quasi-steady state to be reached, the disk must be viscously relaxed. Depending on the initial conditions, quasi-steady state can be reached on a few viscous times as measured at the cavity or tens of times longer if the initial condition is far from the steady state.

3. SIMULATIONS OF CIRCUMBINARY ACCRETION: KEY RESULTS

In this section, we summarize the key findings from recent simulations. Our discussion is guided by our own simulation results using AREPO (Muñoz & Lai 2016; Muñoz et al. 2019, 2020; Siwek et al. 2022) and related work using PLUTO (Miranda et al. 2017), but we compare with the results from other simulations when relevant and discuss more recent progress. AREPO (Springel 2010, Pakmor et al. 2016) is a quasi-Lagrangian Godunov-type moving mesh code. It has an unstructured moving grid with adaptive resolution, and hydrodynamical equations are solved in the moving frame. AREPO was been adapted for viscous accretion disk simulations by Muñoz et al. (2014, 2015). In our work on circumbinary accretion, we simulate 2D Newtonian viscous flow, with a locally isothermal equation of state (EOS) $P = \Sigma c_s^2$, where the sound speed $c_s(r)$ is a prescribed function of r—we assume the disk has a constant disk aspect ratio $h \equiv H/r$. We use the Shakura–Sunyaev α prescription for the viscosity $\nu(r)$. Our typical simulations resolve accretion onto individual binary components down to $0.02a_b$.

In the following, we first consider binaries with mass ratio $q_b \sim 1$ and disks with $H/r \sim 0.1$ and viscosity parameter $\alpha = 0.05$–0.1. We examine both "infinite" disks (with a fixed mass supply rate at $r_{out} \gg a_b$) and finite disks. Later in this section, we discuss how the results vary for different parameters as well as various complications.

3.1. Short-Term Accretion Variability

For an extended disk, when the gas supply rate $\dot{M}_0$ at large distances is constant, the whole binary–disk system can reach a quasi-steady state, in the sense that the time-averaged accretion rate across the CBD and total mass accretion rate onto the binary, $\langle \dot{M}_b \rangle = \langle \dot{M}_1 \rangle + \langle \dot{M}_2 \rangle$, are equal to $\dot{M}_0$. However, the flow rates onto the inner binary cavity and onto individual binary components are highly variable on the binary orbital timescale (Muñoz & Lai 2016, Miranda et al. 2017):

- For nearly circular binaries (with $e_b \lesssim 0.05$), the accretion rates $\dot{M}_1$ and $\dot{M}_2$ vary with a dominant period of about $5P_b$ (where P_b is the binary orbital period), a result that was already found in earlier simulations (e.g., MacFadyen & Milosavljević 2008, Shi et al. 2012, D'Orazio et al. 2013). This dominant period corresponds to the Kepler period of gas at the inner edge of the disk, $r_{cav} \simeq 3a_b$. The reason for this is that for circular binaries, the accretion onto the inner cavity arises from the development of $m = 1$ lumps at the inner disk edge, and the lump has a pattern speed equal to the local Kepler velocity (see **Figure 3**).
- For $e_b \gtrsim 0.05$, the dominant variability of $\dot{M}_1$ and $\dot{M}_2$ has a period of P_b. The reason is that for eccentric binaries, the mass transfer onto the cavity mainly occurs when the binary is at apocenter, where the binary component is closest to the disk inner edge and "grabs" the gas from the disk and funnels it inward (see **Figure 4**).

The different variability timescales (P_b versus $5P_b$) are important when trying to infer the orbital period of binary MBHs from the observed variability of dual AGNs (see Section 4). These short-term variabilities can be also used to confront observations of T Tauri binaries (e.g., Tofflemire et al. 2017a,b, 2019). In some cases, the effective sizes (which can be different from the stellar radii because of the magnetic fields) of the individual accretors can be constrained.

3.2. Longer-Term Accretion Variability

Binary accretion can vary on a timescale much longer the binary orbital period (**Figure 2**), even when the mass supply rate $\dot{M}_0$ is constant. For an equal-mass circular binary, the accretion rates onto individual stars are quite similar to each other, following the same variable pattern in time,

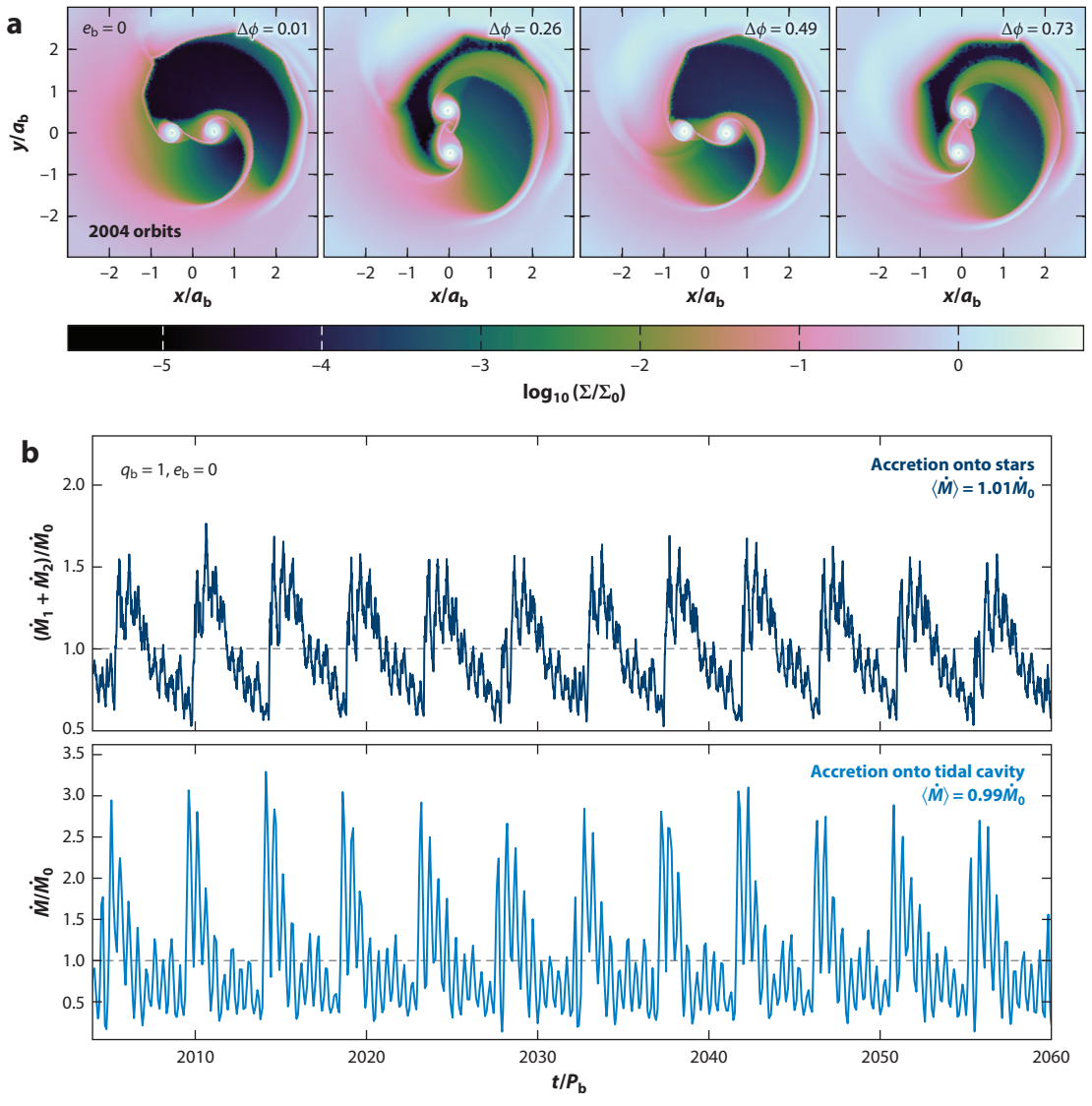

Figure 3

Short-term variability of circumbinary accretion for an equal-mass ($q_b = 1$) circular binary ($e_b = 0$) with $h = 0.1$ and $\alpha = 0.1$. (*a*) Surface density field evolution within timescales of about one binary orbit at $2{,}004 + \Delta\phi$ orbits. In this case, the pattern repeats every half orbit. (*b*) Accretion rate onto the binary and at the inner edge of the circumbinary disk; both exhibit bursty behaviors with a dominant period of about $5P_b$. Figure adapted with permission from Muñoz & Lai (2016); copyright 2016 AAS.

as illustrated in **Figure 5*a***. By contrast, for eccentric binaries, one of the binary components can accrete at a rate 10–20 times greater than its companion, even for mass ratio $q_b = 1$, as illustrated in **Figure 5*b***.

This "symmetry breaking" between the binary components, however, does not persist. Instead, it alternates over timescales on the order of $200P_b$ (Muñoz & Lai 2016; see also Dunhill et al. 2015). This long-term quasi-periodicity can be attributed to a slowly precessing, eccentric CBD. Indeed, the inner region of the disk generally develops eccentricity and precesses coherently (see below).

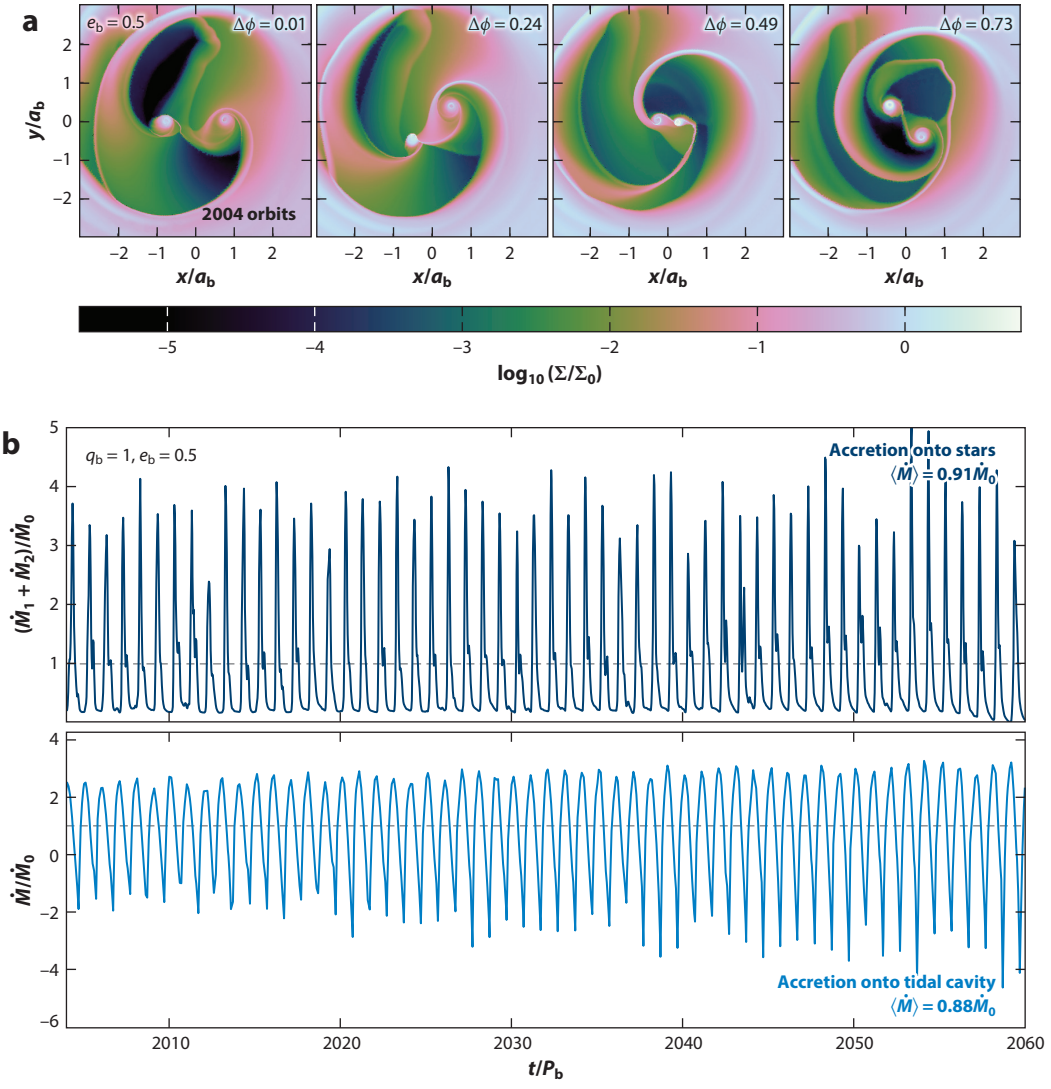

Figure 4

Same as **Figure 2**, except for an eccentric binary with $e_b = 0.5$. The accretion rate exhibits pulsation with a dominant period of P_b. Note that in panel *a*, there is an asymmetry in the density field. This is related to the way gas is funneled into the central cavity. At a given time, an eccentric inner disk could favor one star over the other; but the accretion rate asymmetry is reversed after hundreds of binary orbits. Figure adapted with permission from Muñoz & Lai (2016); copyright 2016 AAS.

The apsidal precession rate of an eccentric ring (of radius r) around the binary is given by

$$\dot{\varpi}_d \simeq \frac{3\Omega_b}{4}\frac{q_b}{(1+q_b)^2}\left(1+\frac{3}{2}e_b^2\right)\left(\frac{a_b}{r}\right)^{7/2}. \qquad 10.$$

At $r \sim 3a_b$ (the cavity radius), this corresponds to a period of 200–$300P_b$. Over longer timescales ($\gg 200P_b$), the net accretion rates onto individual binary components are the same (for $q_b = 1$).

This symmetry breaking behavior (even for $q_b = 1$) is interesting in connection to AGNs around massive black hole binaries (MBHBs) or similar accretion phenomena around binary

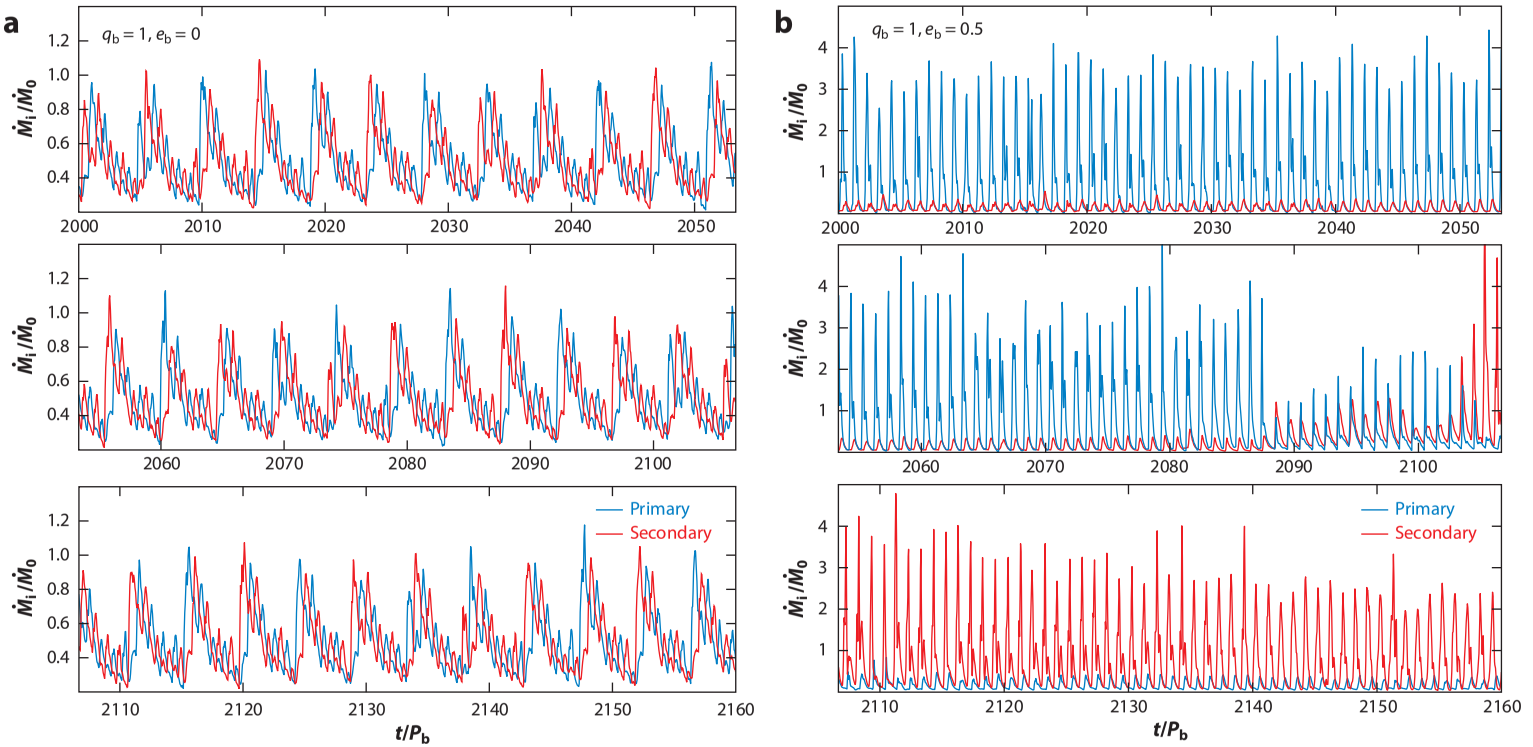

Figure 5

Accretion rates onto the primary and secondary members of the binary, $\dot{M}_1$ and $\dot{M}_2$ in blue and red, respectively, for an equal-mass binary ($q_b = 1$). Panels show the cases of (*a*) $e_b = 0$ and (*b*) $e_b = 0.5$. The eccentric binary experiences a symmetry breaking, with one star accreting between 10 and 20 times more mass than its companion. This trend, however, is reversed at $t \sim 2110 P_b$ and then reversed back at $t \sim 2250 P_b$. The individual accretion rates eventually average out to $\langle \dot{M}_1 \rangle = \langle \dot{M}_2 \rangle = 0.5 \dot{M}_0$. Figure adapted with permission from Muñoz & Lai (2016); copyright 2016 AAS.

T Tauri stars. This behavior implies that even when the two binary components are very similar in mass, accretion may predominantly occur in one of components and last for hundreds of orbits. Interestingly, Tofflemire et al. (2019) has reported evidence for preferential accretion onto the primary of the T Tauri Binary TWA 3A, in contradiction with expectations that accretion should be preferential onto the secondary (see Section 3.6 below). Having an eccentricity of $e_b = 0.67$ (Tofflemire et al. 2017b), TWA 3A could be an example of this intriguing behavior.

3.3. Disk Eccentricity and Precession

Numerical simulations have long shown that eccentricity can develop in the innermost region of the CBD (MacFadyen & Milosavljević 2008, Miranda et al. 2017). Although this is most noticeable by the formation of a lopsided tidal cavity (e.g., Kley & Dirksen 2006, Thun et al. 2017, Ragusa et al. 2020), it responds to a phenomenon of much wider extent. Indeed, disk eccentricity e_d can be significant ($\gtrsim$0.01) out to radii of ∼10–15 a_b (Miranda et al. 2017, Muñoz & Lithwick 2020). Typically, this inner region undergoes coherent apsidal precession, with the rate given by the appropriate spatial average of Equation 10 (see below). But in some cases, it can also become apsidally locked relative to the binary's eccentricity vector, as found in the $0.2 \lesssim e_b \lesssim 0.4$ equal-mass binary simulations of Miranda et al. (2017) and in the unequal-mass eccentric binary simulations of Siwek et al. (2022). An example of the coherent precession of a CBD and its correspondence to a lopsided cavity is illustrated in **Figure 6**.

The coherence of inner CBD precession requires efficient communication between different disk regions (recall that the apsidal precession rate of a test particle around the binary depends strongly on r; see Equation 10). In the absence of disk self-gravity, this communication is achieved

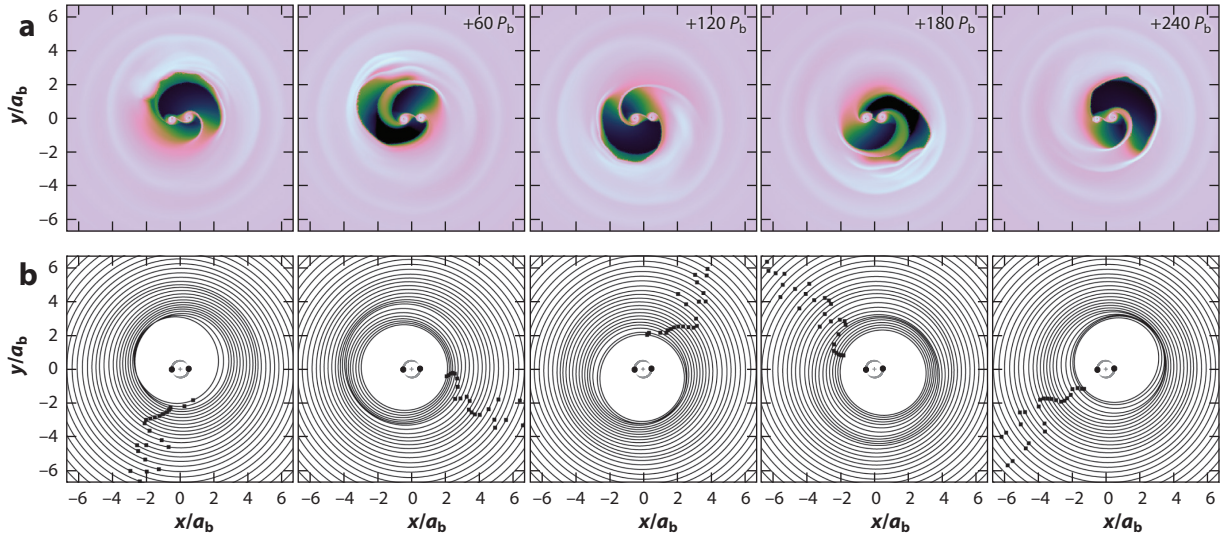

Figure 6

Evolution of circumbinary disks over secular timescales. (*a*) Surface density (logarithmic scale) in the vicinity of a binary with $q_b = 1$ and $e_b = 0$ (disk parameters are $h = \alpha = 0.1$) in intervals of 60 binary orbits once steady state has been achieved. The gas morphology is consistent throughout the panels except for the orientation of the central cavity, which evolves in tandem with the disk eccentricity. (*b*) Barycentric elliptical "orbits" corresponding to gas eccentricity binned in semimajor axis. These "orbits" change in time, exhibiting prograde apsidal precession, as evidenced by the advancement of the longitude of pericenter ϖ_d, depicted by solid black squares; the orientation of the ellipses is roughly coherent (ϖ_d is approximately equal for all radii) out to a distance of ∼10a_b from the barycenter. Figure adapted with permission from Muñoz & Lithwick (2020); copyright 2020 AAS.

by gas pressure, which induces disk precession that balances the forced precession (Equation 10; Goodchild & Ogilvie 2006, Teyssandier & Ogilvie 2016). The eccentricity profile of the CBD actually corresponds to the eigenmode of a Schrödinger-like eccentricity equation of Goodchild & Ogilvie (2006; see also Shi et al. 2012; Teyssandier & Ogilvie 2016; Lee et al. 2019a,b; Muñoz & Lithwick 2020), and the global disk precession frequency is the associated eigenfrequency. The mode is trapped between two turning points that result from the sharply truncated CBD; as a result, most of the mode "lives" in the immediate vicinity of the cavity, thus obeying the local precession law (with the mode frequency approximately equal to $\dot{\varpi}_{\rm d}$ evaluated at the cavity radius; Muñoz & Lithwick 2020). Interestingly, the mode is so strongly confined that pressure-induced precession plays a minor role.

Although the eccentricity profile and precession frequency can be understood via a linear analysis, the actual amplitude of the eccentricity eigenmode depends on the details of eccentricity growth, damping, and saturation. The growth of eccentricity likely results from a combination of the direct "hydraulic pumping" from high Mach number streamers colliding directly with the inner edge of the disk, as argued by Shi et al. (2012), and the tidal excitation via eccentric Lindblad resonances (ELRs; e.g., Hirose & Osaki 1990; Lubow 1991a,b). An ELR is a parametric instability arising from the modulation of the disk particle's epicyclic motion by the binary potential. As discussed in Section 2, the gravitational potential from the binary on the disk can be decomposed into many harmonic components, each having a pattern rotation frequency $\omega_{\rm p} = \omega_{mn} = N\Omega_{\rm b}/m$, where m and $N = 1, 2, \ldots$ (and $n = N - m$). In the presence of this rotating potential, the epicyclic frequency κ of a disk fluid element attains a modulation term proportional to $\cos m(\omega_{\rm p} - \Omega)t$ (where Ω is the angular frequency of the disk). A parametric resonance occurs when $m(\omega_{\rm p} - \Omega) \simeq 2\kappa \simeq 2\Omega$, i.e.,

$$\frac{\Omega(r_{\rm ELR})}{\Omega_{\rm b}} = \frac{N}{m+2}. \qquad 11.$$

The strength of the forcing depends on $e_{\rm b}$, with the components $m = 2$ and $N = 1$ (which has $\Phi \propto e_{\rm b}$, and $m = 2$ and $N = 2$ [with $\Phi \propto (1 - 5e_{\rm b}^2/2)$] being the most important. (See the sidebar titled Eccentric Lindblad/Corotation Resonances and Mean-Motion Resonances.)

For a binary with finite eccentricity, the secular (orbital-averaged) interaction can also drive the disk eccentricity. If we define the complex eccentricity $\mathcal{E}_{\rm d}(r,t) = e_{\rm d}(r,t)\exp[i\varpi_{\rm d}(r,t)]$ for the

ECCENTRIC LINDBLAD/COROTATION RESONANCES AND MEAN-MOTION RESONANCES

The term ELRs is often used to describe Lindblad resonances that are associated with eccentricities. ELRs and "eccentric corotation resonances" are related to mean-motion resonances in celestial mechanics (Murray & Dermott 1999) as follows. Consider the perturbation with a pattern rotation frequency $\omega_{mn} = (m\Omega_{\rm b} + n\kappa_{\rm b})/m$ (see Equation 2). A general Lindblad/corotation resonance occurs when

$$m(\omega_{mn} - \Omega) = n'\kappa,$$

where $n' = 0$ gives the corotation resonance, and $n' = \pm 1$ gives the (linear) LRs, and $|n'| > 1$ would involve nonlinear resonances. Using $\kappa_{\rm b} = \Omega_{\rm b} - \dot{\varpi}_{\rm b}$ and $\kappa = \Omega - \dot{\varpi}$, where $\dot{\varpi}_{\rm b}$ and $\dot{\varpi}$ are the apsidal precession rates of the binary and the disk, respectively, the above resonance condition becomes

$$(m+n)\Omega_{\rm b} - n\dot{\varpi}_{\rm b} - (m+n')\Omega + n'\dot{\varpi} = 0.$$

This describes the $(m+n):(m+n')$ mean-motion resonance, and the strength of the interaction potential is $\propto e_b^{|n|}e^{|n'|}$.

disk particle (at radius r) and $\mathcal{E}_b = e_b \exp(i\varpi_b)$ for the binary, then the secular contribution to the time evolution of $\mathcal{E}_d$ is given by

$$\left(\frac{d\mathcal{E}_d}{dt}\right)_{sec} = i\omega_{db}\mathcal{E}_d - i\nu_{db}\mathcal{E}_b. \quad 12.$$

The apsidal precession rate $\omega_{db} = \dot{\varpi}_d$ (see Equation 10) is driven primarily by the quadrupole potential of the binary, whereas the eccentricity forcing rate ν_{db} is driven by the octupole potential and is given by (e.g., Moriwaki & Nakagawa 2004, Miranda et al. 2017)

$$\nu_{db} \simeq \frac{15\,\Omega_b}{16}\frac{q_b(1-q_b)}{(1+q_b)^3}\left(1+\frac{3}{4}e_b^2\right)\left(\frac{a_b}{r}\right)^{9/2}. \quad 13.$$

In the presence of an eccentricity-damping force (and neglecting other hydrodynamical effects), this secular forcing tends to drive the disk toward a "forced" eccentricity, given by $\mathcal{E}_d = (\nu_{db}/\omega_{db})\mathcal{E}_b$; this forced eccentricity is apsidally aligned with the binary eccentricity.

Thus, the eccentricity evolution of the CBD around an eccentric binary can be quite complex, driven by the secular and resonant forcings from the binary and hydrodynamical effects. Simulations show that the disk generally exhibits apsidal precession, but the precession rate may not be constant and the line of apses can vary with r. In analogy to a test particle orbit, the CBD should evolve according to coexisting "free" and "forced" modes (e.g., see Lubow 2022). In some cases, the CBD can lock onto the binary and stop precessing altogether (Miranda et al. 2017, Siwek et al. 2022).

3.4. Angular Momentum Transfer and Orbital Evolution: Circular Binaries

We now discuss the important problem of long-term angular momentum exchange between the disk and the binary. Without accretion, the binary always loses angular momentum to the CBD through gravitational (Lindblad) torque. With accretion, the net torque becomes uncertain. As discussed above, the mass flow rate across the disk, $\dot{M}(r,t)$, and the mass accretion rate onto the binary, $\dot{M}_b(t) = \dot{M}_1(t) + \dot{M}_2(t)$, are all highly variable. For an extended disk with a constant supply rate $\dot{M}_0$ at $r = r_{out} \gg a_b$, a quasi-steady state is eventually reached, where the time-averaged mass flow rate is $\langle\dot{M}(r,t)\rangle = \langle\dot{M}_b(t)\rangle = \dot{M}_0$. In general, the net torque on the binary can be obtained in two ways:

- First, it can be computed directly as the sum of the gravitational torque from all the gas plus the accretion torque (due to momentum of the accreting gas onto each binary component), i.e.,

$$\langle\dot{J}_b\rangle = \langle\dot{L}_b\rangle_{grav} + \langle\dot{L}_b\rangle_{acc} + \langle\dot{S}_1\rangle_{acc} + \langle\dot{S}_2\rangle_{acc}. \quad 14.$$

  When the size of the binary component is much less than a_b, the spin torques $\langle\dot{S}_1\rangle$ and $\langle\dot{S}_2\rangle$ are negligible, and the total torque $\langle\dot{J}_b\rangle$ acts on the binary orbit, i.e., $\langle\dot{J}_b\rangle \simeq \langle\dot{L}_b\rangle = \langle\dot{L}_b\rangle_{grav} + \langle\dot{L}_b\rangle_{acc}$.
- Second, the angular momentum flow rate in the CBD (at radius r in the disk) can be computed as (Miranda et al. 2017)

$$\dot{J}(r,t) = \dot{J}_{d,adv} - \dot{J}_{d,visc} - \dot{J}_{d,grav}, \quad 15.$$

  where $\dot{J}_{d,adv}$ is the inward angular momentum advection rate, $\dot{J}_{d,visc}$ is the outward viscous angular momentum transfer rate, and $\dot{J}_{d,grav}$ is the torque from the binary acting on the gas exterior to radius r.

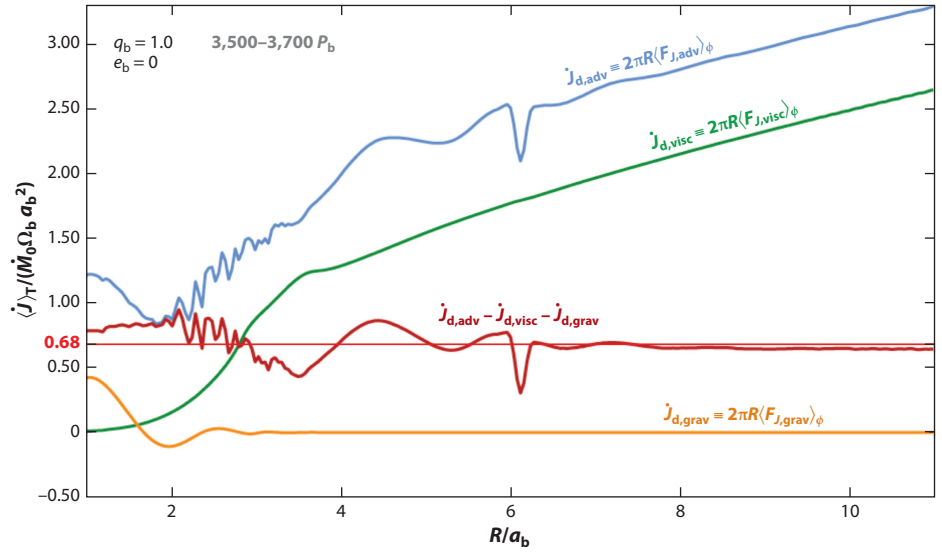

Figure 7

Time-averaged angular momentum flow rate due to advection, viscosity, and gravitational torques in the circumbinary disk, for binary parameters $q_b = 1$ and $e_b = 0$. The total angular momentum flow rate across the disk (*red curve*) is approximately constant, indicating quasi-steady state. For reference, the net torque on the binary $\langle \dot{J}_b \rangle = 0.68 \dot{M}_0 \Omega_b a_b^2$ is overlaid as a straight red line. The "blip" at $r = 6a_b$ and fluctuations at $r \sim 2.5a_b$ are artifacts of the mapping from the Voronoi cells (used in the AREPO code) onto a regular polar grid. Figure adapted with permission from Muñoz et al. (2019); copyright 2019 AAS.

When the disk reaches a quasi-steady state, the time average $\langle \dot{J}(r,t) \rangle$ is independent of r, and the CBD has two global constants: $\langle \dot{M}(r,t) \rangle = \dot{M}_b = \dot{M}_0$ and $\langle \dot{J}(r,t) \rangle = \langle \dot{J}_b \rangle$.

Using long-term AREPO simulations, Muñoz et al. (2019) demonstrated that the global quasi-steady state can be achieved for circumbinary accretion, and $\langle \dot{J}_b \rangle$ values computed using both methods are in agreement (see **Figure 7**). For equal-mass circular binaries (and with $h = 0.1$, and $\alpha = 0.1$), the specific angular momentum "eigenvalue" (i.e., the angular momentum transferred to the binary per unit accreted mass) is

$$l_0 \equiv \frac{\langle \dot{J}_b \rangle}{\langle \dot{M}_b \rangle} = 0.68 a_b^2 \Omega_b, \qquad (q_b = 1,\ e_b = 0), \tag{16.}$$

where $\Omega_b = (GM_b/a_b^3)^{1/2}$ is the rotation rate of the binary. The result was confirmed independently by Moody et al. (2019) using the ATHENA++ code. [A similar positive value of l_0 was first obtained by Miranda et al. (2017) based on PLUTO simulations with an excised cavity.]

For a binary accreting from a finite-sized disk/torus, a global quasi-steady state obviously does not exist. Instead, the accretion proceeds in two phases: an initial transient phase, corresponding to the filling of the binary cavity, followed by a viscous pseudostationary phase (achieved after the viscous time r^2/ν at a few disk radii), during which the torus viscously spreads and accretes onto the binary. In the transient phase, the torque on the binary is negative because it is entirely gravitational (see Section 2). Muñoz et al. (2020) demonstrated that in the viscous phase, the net torque on the binary per unit accreted mass is close to l_0, which is the value derived for "infinite" disks. Because no global steady state is required, this method allows for a more efficient computation of the net torque on the binary in nonsteady situations (i.e., when $\langle \dot{M}_b \rangle$ gradually evolves in time).

Using angular momentum conservation, $dJ_b/dt = \langle \dot{M}_b \rangle l_0$ with $J_b = \mu_b a_b^2 \Omega_b$, we have, for a $q_b = 1$ binary,

$$\frac{\dot{a}_b}{a_b} = 8\left(\frac{l_0}{a_b^2\Omega_b} - \frac{3}{8}\right)\frac{\langle \dot{M}_b \rangle}{M_b}. \quad 17.$$

Thus, the binary orbit expands at the rate $\dot{a}_b/a_b \simeq 2.44\,\langle \dot{M}_b \rangle/M_b$. Note if we take account of the small amount of spin torque $\dot{S}_b = \dot{S}_1 + \dot{S}_2$, the actual $\dot{L}_b$ is a bit smaller than $\dot{J}_b$, and the resulting $\dot{a}_b/a_b$ is then smaller [Muñoz et al. (2019) found $\dot{S}_b \simeq 0.028\dot{M}_b a_b^2 \Omega_b$ when assuming a "stellar" radius of $0.02a_b$, and thus $\dot{a}_b/a_b \simeq 2.2\dot{M}_b/M_b$.]

3.4.1. Lessons from numerical studies of long-term binary evolution. Until recently, it has always been thought that circumbinary accretion leads to binary orbital decay. Pringle (1991) suggested that the strong gravitational torque from the binary on the CBD prevents accretion, and therefore the binary loses angular momentum to the disk (see Section 2). Gas accretion changes the picture completely. Only a few previous studies addressed the issue of angular momentum transfer in a quantitative way. Examples include MacFadyen & Milosavljević (2008) and Shi et al. (2012), whose simulations excise the inner cavity. MacFadyen & Milosavljević (2008) considered $H/r = 0.1$ and a disk viscosity with $\alpha = 0.01$ and adopted a polar grid in the domain between $r_{in} = a_b$ and $r_{out} = 100a_b$. They found a reduction of mass accretion onto the binary and the dominance of the gravitational torque relative to advective torque (therefore a negative net torque on the binary). However, with their small α parameter, the "viscous relaxation" radius at $t = 4{,}000P_b$ (the typical duration of their runs) is only about $3a_b$, and their surface density profile is far from steady state even at $r \sim r_{in}$. So it is likely that the result of MacFadyen & Milosavljević (2008) reflects a "transient" phase of their simulations. Shi et al. (2012) obtained a positive value of $\dot{J}_b$ in their 3D MHD simulations of CBDs (truncated at $r_{in} = 0.8a_b$). However, the duration of their simulations is only $\sim 100P_b$, and it is unlikely that a quasi-steady state is reached. Their value of l_0, which is too small to cause orbital expansion, may not properly characterize the long-term evolution of the binary. Tang et al. (2017) carried out simulations of accretion onto circular binaries using `DISCO` (Duffell & MacFadyen 2012, Duffell 2016) with $h = 0.1$ and $\alpha = 0.1$. For the accretion prescription, they assumed that inside a "sink" radius (measured from each "star"), the gas is depleted at a rate of $d\Sigma/dt = -\Sigma/t_{sink}$, with t_{sink} being a free parameter. They claimed that the net torque on the binary is negative unless t_{sink} is much less than P_b. This result is in contradiction with those of Muñoz et al. (2019) and Moody et al. (2019); the latter adopted a similar accretion prescription and did not find the same behavior as Tang et al. (2017). More recent works using `DISCO` (Duffell et al. 2020, D'Orazio & Duffell 2021, Dittmann & Ryan 2021) and the Cartesian-grid code `Mara3` (Tiede et al. 2020, Zrake et al. 2021) have produced similar results as those of Muñoz et al. (2019, 2020) and Moody et al. (2019), so it appears that different groups have reached agreement (at least for disks with $h = 0.1$ and $\alpha = 0.1$). See below for a discussion of the numerical resolution requirement to obtain reliable net torques.

3.4.2. Dependence on disk thickness and viscosity. Most of the recent simulations described thus far in this review are 2D, low-mass, viscous accretion disks with a locally isothermal EOS. In this case, the most important parameters are q_b, e_b, α (or ν), and h. Of these, q_b and e_b have been studied most extensively, but h and α can be equally important.

An exploration of the dependence of l_0 and $\dot{a}_b/a_b$ on h for equal-mass, circular binaries was carried out by Tiede et al. (2020). Using the Godunov code `Mara3` (implemented in Cartesian coordinates with static mesh refinement), they varied $h = \{0.02, 0.033, 0.05, 0.1\}$ while fixing the kinematic viscosity $\nu = \sqrt{2} \times 10^{-2} a_b^2 \Omega_b$ (or $\alpha = 10^{-2} h^{-2}$ at $r = 2a_b$). They found that l_0

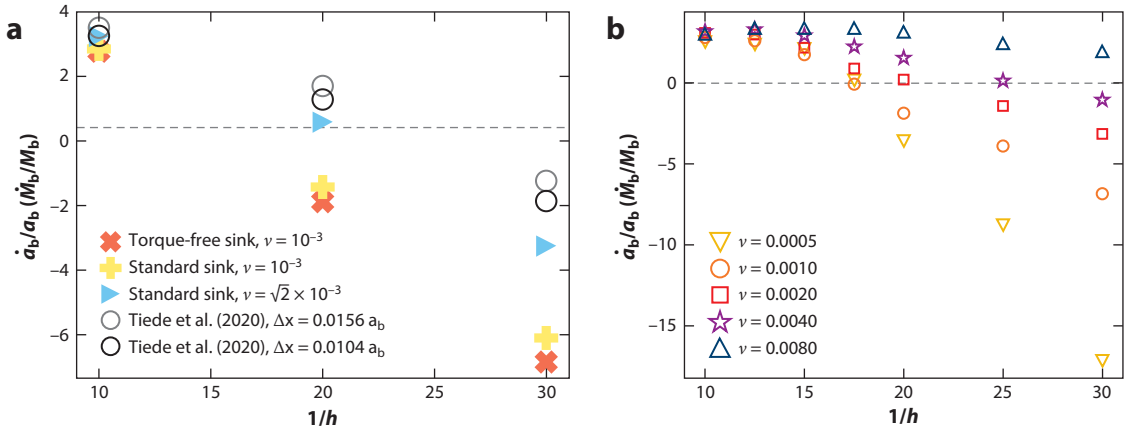

Figure 8

Migration rate $\dot{a}_b/a_b$ in units of $\dot{M}_b/M_b$ as a function of disk aspect ratio h and kinematic viscosity coefficient ν. (*a*) Numerical effects like insufficient resolution and sink prescription can affect the value of l_0, with some results reported by Tiede et al. (2020) being nonconverged, but the transition from outward to inward migration at $h \simeq 0.04$ appears to be robust. (*b*) The direction of migration depends on h and on the (globally constant) value of ν, with the small-ν systems migrating inward more rapidly than the more viscous ones. This difference grows as h is decreased. Figure adapted with permission from Dittmann & Ryan (2022); copyright 2022 AAS.

monotonically decreases with decreasing h and that l_0 falls below $(3/8)a_b^2\Omega_b$ (see Equation 17) when $h \lesssim 0.04$. This occurs in spite of the CBD mean cavity remaining roughly the same size (because they use constant ν instead of constant α, the truncation estimate in Miranda & Lai 2015 would yield identical cavity sizes), albeit the streamers become more erratic, narrow, and denser than in thicker disks. The authors reported a dependence of the results on resolution, which is likely due to the poorly resolved CSDs even with mesh refinement. Dittmann & Ryan (2022) carried out follow-up work using a version of `DISCO` and found that the Tiede et al. (2020) results were likely unconverged but qualitatively confirmed the migration transition at $h = 0.04$. Dittmann & Ryan (2022) also explored the role of viscosity. Whereas earlier works (Duffell et al. 2020, Muñoz et al. 2020) found that the $h = 0.1$ simulations exhibited little dependence on viscosity, when h is varied, lower viscosity appears to further reduce l_0 with decreasing h (see **Figure 8*b***). The role played by disk thickness could introduce a crucial distinction between the young stellar binaries accreting from protostellar disks and MBHBs accreting from AGN disks. Whereas the former systems can be well represented by disks with $h \sim 0.1$, the latter are better characterized by values of $h \sim 10^{-2}$ or less (Sirko & Goodman 2003, Thompson et al. 2005).

Two difficulties must be addressed when discussing the roles of disk viscosity and aspect ratio. First, a low-viscosity disk simply takes longer to reach a quasi-steady state (Miranda et al. 2017, Muñoz et al. 2020, Dittmann & Ryan 2022), and this is likely the culprit of simulations reporting suppressed binary accretion at low viscosities (e.g., Ragusa et al. 2016). To obtain reliable results, simulations often need an iterative reassessment of the initial condition (Miranda et al. 2017, Dempsey et al. 2020a). Second, the resolution requirements in the CSDs have not been rigorously addressed, and these can be very stringent. Insufficient resolution would dilute the strong spiral arms in the CSDs, which are the source of positive torques opposing the negative torque from the CBD and the streams. And the width of these spiral arms can be very sensitive to the choice of h. Borrowing a page from the theory of planet–disk interaction (e.g., see Papaloizou et al. 2007), we know that the one-sided Lindblad torque peaks at an azimuthal number of $\sim 1/(2h)$ (Ward 1997) and the width of a spiral arm is $\sim 4\pi r h^2$ (e.g., Masset 2008), setting a minimum resolution

requirement for the adequate torque calculation. Although this resolution requirement can be easily met by modern simulations in the CBD region, it can become extremely difficult in the CSD region, where the number of resolution elements per radial interval around each accretor can be rather small. Furthermore, in the frame of the moving accretor, the computational grid is never of a polar nature and, in many cases, is effectively Cartesian at the CSDs scales. Consequently, numerical diffusion can become very taxing in the CSDs, especially for low values of h, where the spiral arms are narrow. Under-resolving these spiral arms has the unwanted consequence of reducing the positive torque stemming from this region, favoring the (well-resolved) negative torques from the CBD.

Recent SPH simulations carried out by Heath & Nixon (2020) exhibit a drastically different torque reversal threshold of $h = 0.2$. However, these simulations do not exhibit any substantial CSD formation and are thus prone to underestimate the positive torque stemming from the CSD region. Franchini et al. (2022) showed that the SPH code `PHANTOM` can only reproduce the results of Muñoz et al. (2019) if the CSD structure is properly resolved with the use of 10^7 particles. In contrast, they confirmed that the meshless particle-based code `GIZMO` (Hopkins 2015) can produce outward migration if the number of resolution elements is increased within the cavity region.

3.5. Long-Term Orbital Evolution: Eccentric Binaries

The secular binary migration rate of Equation 17 assumes that $e_b = 0$ at all times. For general eccentric binaries, Muñoz et al. (2019) devised a method to compute from simulations both dl_b/dt and $d\mathcal{E}_b/dt$, where $\mathbf{l}_b = \mathbf{r}_b \times \mathbf{v}_b$ (with $\mathbf{r}_b = \mathbf{r}_1 - \mathbf{r}_2$ being the binary separation vector, and $\mathbf{v}_b = d\mathbf{r}_b/dt$) and $\mathcal{E}_b = \frac{1}{2}\mathbf{v}_b \cdot \mathbf{v}_b - GM_b/|\mathbf{r}_b| = -GM_b/(2a_b)$ are the specific orbital angular momentum and energy of the binary, respectively. In particular, the energy transfer rate can be computed from

$$\frac{d\mathcal{E}_b}{dt} = -\frac{G\dot{M}_b}{r_b} + \mathbf{v}_b \cdot (\mathbf{f}_1 - \mathbf{f}_2), \tag{18.}$$

where $\mathbf{f}_1 = \mathbf{f}_{1,\mathrm{grav}} + \mathbf{f}_{1,\mathrm{acc}}$ is the force per unit mass on M_1 (from gravity and accretion), and similarly for $\mathbf{f}_2$. From these, one can obtain the orbital evolution rates

$$\frac{\dot{a}_b}{a_b} = -\frac{\dot{\mathcal{E}}_b}{\mathcal{E}_b} + \frac{\dot{M}_b}{M_b}, \tag{19.}$$

$$-\frac{2e_b\dot{e}_b}{1-e_b^2} = 2\frac{\dot{l}_b}{l_b} + \frac{\dot{\mathcal{E}}_b}{\mathcal{E}_b} - 2\frac{\dot{M}_b}{M_b}. \tag{20.}$$

The results of Muñoz et al. (2019) are shown in **Figure 9**. They concluded that equal-mass binaries of different eccentricities expand at the rate of $\dot{a}_b/a_b \sim \dot{M}_b/M_b$ (**Figure 9*a***). But while $\dot{a}_b/a_b$ is always positive, the nonmonotonic feature of $\dot{a}_b/a_b$ as a function of e_b is of interest. Related to this feature is the evolution of e_b: Muñoz et al. (2019) found that $\dot{e}_b$ (**Figure 9*b***) is slightly negative for $e_b \sim 0$, becomes positive at $e_b = 0.1$, and becomes negative again at $e_b \gtrsim 0.5$. Thus it appears that there is an eccentricity "attractor" below $e_b \sim 0.5$ and above $e_b \sim 0.3$. This behavior was confirmed in an independent study by Zrake et al. (2021; see **Figure 9**), who used the `Mara3` code to study accretion from finite-sized disks onto eccentric binaries finely sampling a range of values of e_b and reported an equilibrium binary eccentricity of $e_b \simeq 0.45$. These results are shown in **Figure 9*b*** alongside an associated fitting function. The figure also includes the results of D'Orazio & Duffell (2021) for $\dot{a}_b$ and $\dot{e}_b$, who found agreement with Muñoz et al. (2019) and Zrake et al. (2021) for $\dot{e}_b$ but reported negative $\dot{a}_b$ for intermediate values of e_b. These authors argued that eccentric binaries close to $e_b = 0.4$ are able to migrate inward because of the nonaxisymmetric distortion of the circumbinary cavity for those parameters.

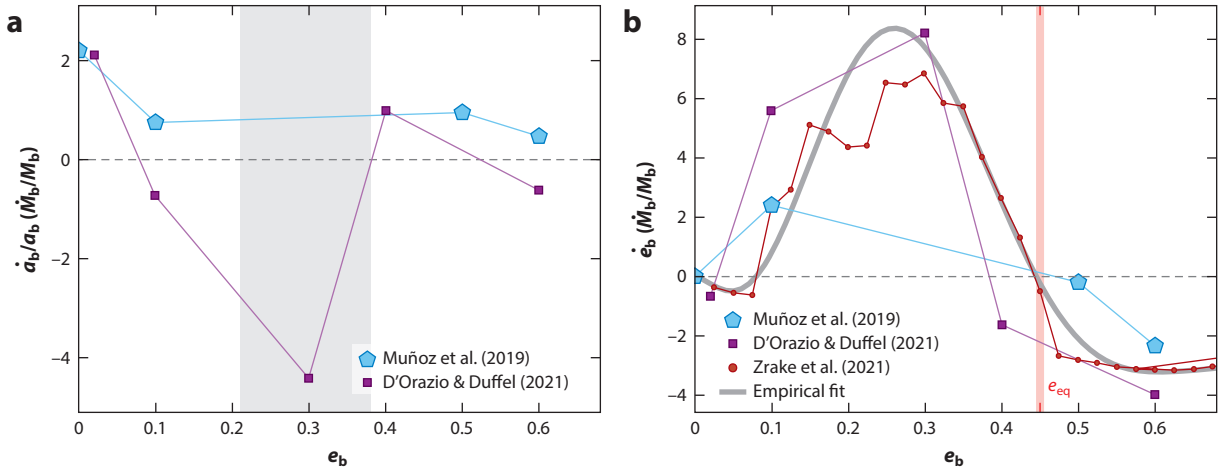

Figure 9

(*a*) Secular rate of change of semimajor axis $(\dot{a}_b/a_b)(\dot{M}_b/M_b) = da_b/d\ln M_b$ for equal-mass binaries at different eccentricities and with the fiducial parameters $h = \alpha = 0.1$. Results from Muñoz et al. (2019) reported outward migration exclusively, whereas D'Orazio & Duffell (2021) reported a window (*gray region*) in which binaries could migrate inward concomitantly with growing in eccentricity. (*b*) Secular rate of change of eccentricity $\dot{e}_b/(\dot{M}_b/M_b) = de_b/d\ln M_b$ of equal-mass binary undergoing circumbinary accretion as a function of the binary eccentricity. Note that $\dot{e}_b$ is negative for $e_b \lesssim 0.08$ and positive for larger e_b, then becomes negative again for $e_b \gtrsim 0.45$. Figure adapted with permission from Zrake et al. (2021); copyright 2021 AAS.

3.6. Accretion onto Unequal-Mass Binaries

Early SPH simulations of young stellar binaries accreting from gaseous environments (e.g., Bate & Bonnell 1997, Bate 2000, Bate et al. 2002) revealed that the accretion flow depends sensitively on the binary mass ratio $q_b = M_2/M_1$, and that even over short timescales, the secondary grows in mass faster than the primary (e.g., Bate 2000). Farris et al. (2014) conducted the first systematic study of circumbinary accretion as a function of q_b for circular binaries using an early version of the code `DISCO`. These simulations confirmed the existence of preferential accretion onto the secondary and also found that the time variability of accretion is a function of q_b. Using a similar setup, Muñoz et al. (2020) carried out `AREPO` simulations for q_b between 0.1 and 1 until a quasi-steady state was reached. Although they found some quantitative discrepancies with Farris et al. (2014), they confirmed that both preferential accretion and the accretion variability depend on q_b.

Currently, a consensus has emerged across simulation studies of accreting circular binaries. For fiducial parameters $h = 0.1$ and $\alpha = 0.1$, the key findings include the following:

- **Accretion is primarily modulated at two frequencies: $\Omega_b/5$ and Ω_b.** For $q_b \geq 0.5$, the accretion variability is dominated by the lower-frequency mode (a period of about $5P_b$); for $q_b \leq 0.4$, it is dominated by the higher-frequency mode (a period of P_b; see **Figure 10**). The switch is associated with the disappearance of the orbiting "lump" at low binary mass ratios.
- **The secondary accretes more than the primary.** The long-term preferential accretion ratio, defined as $\eta = \langle\dot{M}_2\rangle/\langle\dot{M}_b\rangle$, is shown in **Figure 11** from a collection of recent studies. Although some discrepancies remain, the monotonically decreasing trend of η versus q_b is robust. The result of Muñoz et al. (2020) follows an approximately linear relation

$$\frac{\langle\dot{M}_2\rangle}{\langle\dot{M}_b\rangle} \simeq 0.5 + \frac{4}{9}(1 - q_b). \qquad 21.$$

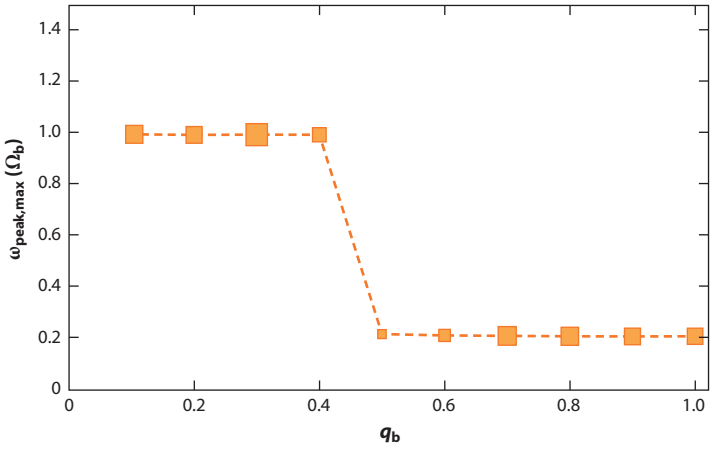

Figure 10

Dominant frequency $\omega_{peak,max}$ (in units of the binary orbital frequency Ω_b) from the spectral analysis of $\dot{M}_b$ for different values of $q_b = M_2/M_1$. The dominant frequency is about $\Omega_b/5$ for $q_b \geq 0.5$, although its power (indicated by the size of the makers) decreases with decreasing q_b. For $q_b \leq 0.4$, the dominant frequencies are Ω_b and its harmonics. Figure adapted from Muñoz et al. (2020); copyright 2020 AAS.

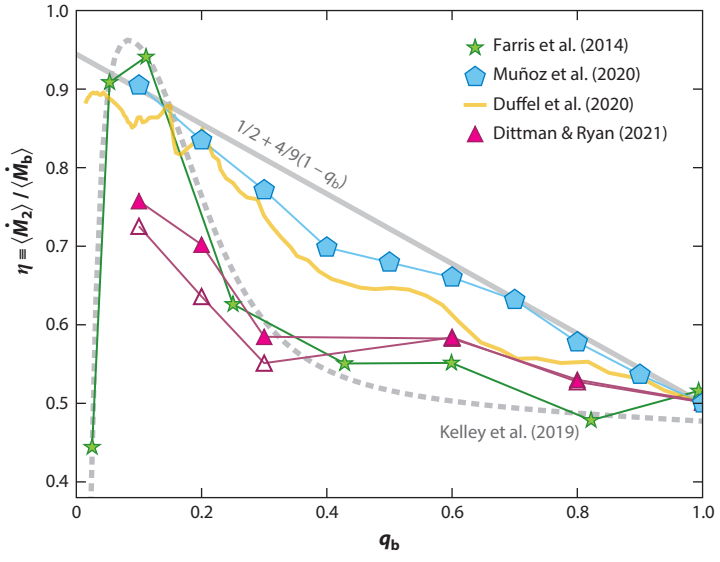

Figure 11

Preferential accretion ratio $\eta \equiv \langle \dot{M}_2 \rangle / \langle \dot{M}_b \rangle$ compiled from the literature for $e_b = 0$ and $h = 0.1$ (viscosity prescription is either constant $\alpha = 0.1$ or constant $\nu = 0.01 a_b^2 \Omega_b$). The data are from Farris et al. (2014; DISCO, α-viscosity), Muñoz et al. (2020; AREPO, α-viscosity), Duffell et al. (2020; DISCO, constant ν), and Dittmann & Ryan (2021; modified DISCO, constant ν; *filled magenta triangles* for standard sinks and *empty triangles* for torque-free sinks). The gray lines depict the Kelley et al. (2019) fit to the Farris data and the linear relation of Equation 21.

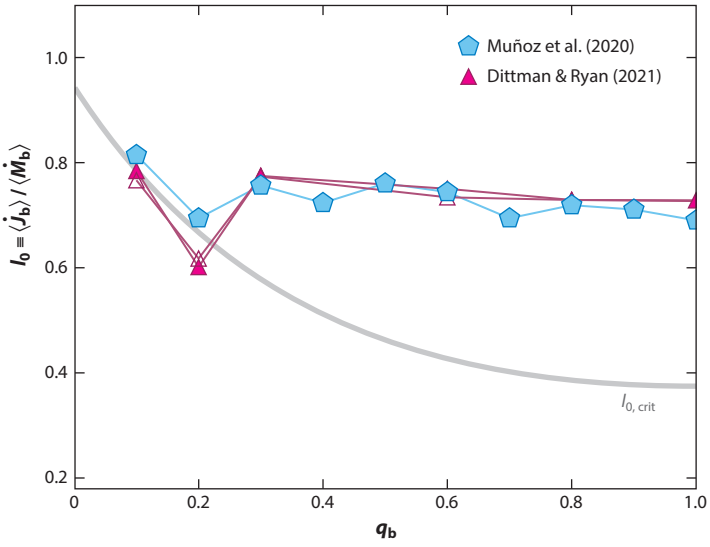

Figure 12

Angular momentum eigenvalue l_0 as a function of the binary mass ratio q_b compiled from the literature for $e_b = 0$ and $h = 0.1$ (the viscosity prescription is either constant $\alpha = 0.1$ or constant $\nu = 0.01 a_b^2 \Omega_b$). The symbols are the same as in **Figure 11**. Note that Duffell et al. (2020) did not report l_0 but only the gravitational torque T_{grav} on the binary; one can obtain the corresponding l_0 from T_{grav} and η by neglecting the spin torques and accretion-induced specific torque.

- **The accretion angular momentum eigenvalue $l_0 = \langle \dot{J}_b \rangle / \langle \dot{M}_b \rangle$ stays around $0.68 a_b^2 \Omega_b$ to $0.8 a_b^2 \Omega_b$ for q_b in the range 0.1 to 1.** **Figure 12** collects the results reported by Muñoz et al. (2020) and Dittmann & Ryan (2021), which are in remarkable agreement. Dittmann & Ryan (2021) further showed that l_0 depends weakly on the sink prescription, provided that the sink region is small enough. Note that this positive eigenvalue does not guarantee binary expansion, as some accreted angular momentum goes into equalizing the binary's mass ratio. For η given by Equation 21, the critical eigenvalue above which orbital expansion occurs is

$$l_{0,\rm crit} = \frac{a_b^2 \Omega_b}{2(1+q_b)^2}\left[1 + q_b + q_b^2 + \frac{8}{9}(1-q_b)^2(1+q_b)\right], \qquad 22.$$

  which reduces to $l_{0,\rm crit} = (3/8) a_b^2 \Omega_b$ for $q_b = 1$. Equation 22 is shown in **Figure 12** and hints at binary contraction for $q_b \approx 0.1$.
- **The binary orbit expands at a nearly constant rate of $\langle \dot{a}_b \rangle / a_b \simeq 2 \langle \dot{M}_b \rangle / M_b$ for $0.3 \le q_b \le 1$; this rate becomes significantly smaller for $q_b \le 0.2$ and changes sign for $q_b \lesssim 0.1$.** **Figure 13*a*** shows the binary migration rate as computed by Muñoz et al. (2020). As $l_{0,\rm crit}$ grows for small q_b (**Figure 12**), $\langle \dot{a}_b \rangle$ approaches zero, hinting at a reversal of binary migration. Duffell et al. (2020) probed this transition by running `DISCO` simulations that dynamically update the value of q_b, covering values down to $q_b = 10^{-3}$. They found that the net gravitational torque becomes negative for $q_b \lesssim 0.05$, implying inward migration. Recent results by Dempsey et al. (2021) for $q_b \ll 1$ suggest that this torque reversal transition depends on the dimensionless parameter[1] $K' \equiv q_b^2/(\alpha h^3)$ and is associated with the disk becoming eccentric. For $h = 0.05$ and $\alpha = 10^{-3}$, Dempsey et al. (2021) report that the

[1]The parameter K' has been found to accurately predict the gap width in simulations of planet–disk interaction (i.e., when $q_b \ll 1$; see Kanagawa et al. 2016, Dempsey et al. 2020a).

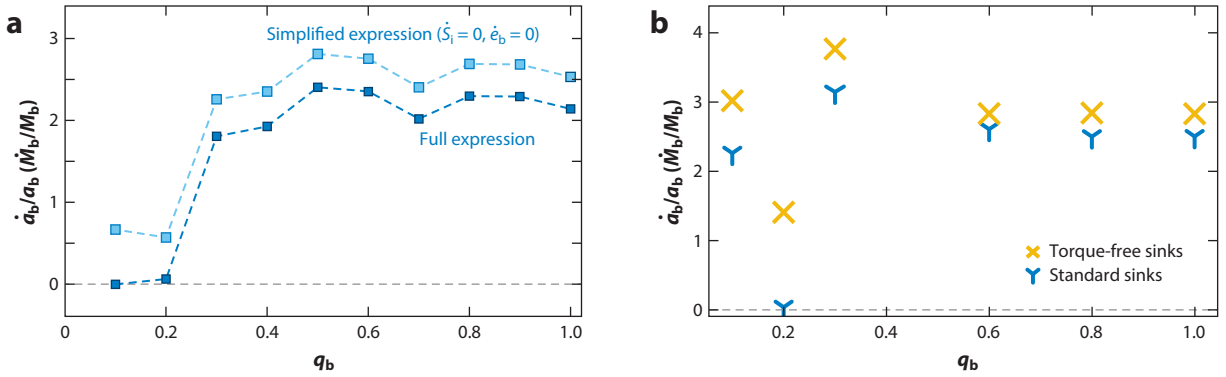

Figure 13

Binary orbital expansion rate $\dot{a}_b/a_b$ (in units of $\dot{M}_b/M_b$) for $e_b = 0$ and $h = 0.1$ (viscosity prescription is either constant $\alpha = 0.1$ or constant $\nu = 0.01 a_b^2 \Omega_b$). (*a*) Results of Muñoz et al. (2020), who computed $\langle \dot{a}_b \rangle$ in two ways: from the energy transfer Equation 19 (*dark blue*) and from angular momentum transfer assuming $\langle \dot{L}_b \rangle \simeq \langle \dot{J}_b \rangle = l_0 \langle \dot{M}_b \rangle$ (*light blue*). (*b*) Results of Dittmann & Ryan (2021), who computed $\langle \dot{a}_b \rangle$ using two sink prescriptions: a standard method (*blue* "*Y*" *symbols*) in which material and linear momentum are removed at the same rate (hence exerting a torque on the gas) and the torque-free method of Dempsey et al. (2020b; *yellow* "*X*" *symbols*), in which the azimuthal momentum of the gas is preserved after mass removal. These results show that sink particles/mass removal algorithms play a minor role when resolution is sufficiently high or sinks are sufficiently small. Panel *a* adapted with permission from Muñoz et al. (2020); copyright AAS. Panel *b* adapted with permission from Dittmann & Ryan (2021); copyright 2021 AAS.

gravitational torque goes from negative to positive when $q_b \gtrsim 1.5 \times 10^{-3}$, or when K' surpasses 20. For $\alpha > 0.03$ and $h = 0.1$, $K' \gtrsim 20$ is equivalent to $q_b \gtrsim 2 \times 10^{-2}$, in agreement with Duffell et al. (2020).

3.7. Other Complications

In the previous subsections, we reviewed the key results from CBD simulations using idealized equations of state (locally isothermal with constant disk aspect ratio h) and viscosity prescription (α viscosity or constant ν), assuming small (local) disk mass (without disk self-gravity). These assumptions may not always apply to realistic disks.

The locally isothermal EOS is known not to conserve the angular momentum flux carried by density waves (Lin & Papaloizou 2011, Miranda & Rafikov 2019), with a resulting modification of the torque profile in the disk. The effect on the integrated torque, however, is negligible for rapidly cooling disks and amounts to a correction of ∼30% in slowly cooling/adiabatic disks (Miranda & Rafikov 2020). Thus, the net contribution of this effect to the migration of binaries is likely minor, except for the borderline cases.

The locally isothermal EOS assumes an efficient cooling process that instantly brings disk temperature back to equilibrium. Without resorting to radiative transfer, the simplest way to assess the role of gas thermodynamics is to allow the disk temperature to relax toward the equilibrium value over some cooling timescale t_{cool} (usually parameterized using $\beta = \Omega_K t_{cool}$, where Ω_K is the local Kepler frequency). Wang et al. (2022a,b) carried out `ATHENA++` simulations using this β-cooling prescription and found that with a longer cooling time, the accretion variability is gradually suppressed and the morphology of the inner disk becomes more symmetric. They also found that the accretion angular momentum eigenvalue l_0 generally decreases with increasing β, such that an equal-mass, circular binary (with equilibrium $h \sim 0.1$) undergoes orbital decay for $\beta \gtrsim 0.2$, although the details depend on the viscosity prescription.

A more complex behavior is expected to arise from 3D MHD simulations, which are needed to capture viscous dissipation self-consistently. Such MHD simulations for circumbinary accretion

are typically initialized with narrow, finite-supply tori and are run for a small number of orbits. Thus, they are useful for studying short-term accretion variability but may not be adequate for probing the long-term flow behavior and the secular evolution of the central binary. Early MHD simulations of CBDs around quasi-circular binaries (Shi et al. 2012, using a version of the finite difference code ZEUS) and GRMHD (Noble et al. 2012, using HARM3D) were carried out excising the central binary for a run time of 80 binary orbits. These show the similar accretion modulation behavior as 2D viscous hydrodynamics despite the development of MHD turbulence in the disk. More recent efforts have been focused on the general relativistic aspects of CBD evolution, which is important for BH binaries close to merger (with separations of 10–20 gravitational radii). For example, GRMHD simulations using HARM and its variants have been implemented with an approximate analytic metric of binary BHs in order to include the CSDs in the computational domain, although a circular region at the binary barycenter is still excised (Bowen et al. 2017, 2018; Combi et al. 2021, 2022). These simulations (typically run for ∼20 orbits) show additional time modulations that are interpreted as purely relativistic effects.

The simulations discussed in the previous subsections all assume that the local disk mass near the binary is much less than M_b (although the mass of an extended disk can be much larger). When this condition is not satisfied, the flow/binary dynamics and evolution can be quite different. Such massive disks (or "envelopes") naturally occur immediately following galaxy mergers. An MBHB embedded in such an envelope is expected to undergo orbital decay through dynamical friction (e.g., Escala et al. 2005, Cuadra et al. 2009, Franchini et al. 2021). Massive CBDs or envelopes may also be important for the formation of close (AU-scale) protostellar binaries (see Section 4.2). If CBDs are massive enough and no substantial CSDs can form, the binary is bound to lose angular momentum to the gas. Numerical simulations show that small-mass protobinaries embedded in collapsing cores decay in separation quickly (e.g., Bate 2000, Bate et al. 2002). Aided by dynamical friction, the pair becomes bound at small separations and continues to grow until it becomes dynamically dominant. Only then a true CBD may form, at which point the binary may have already reached AU-scale separations. More recent simulations, including the effects of magnetic fields, find qualitatively similar results, except for a further accelerated orbital decay attributed to magnetic braking of the gas envelope (e.g., Zhao & Li 2013, Kuruwita et al. 2020). For example, in the simulations of Kuruwita et al. (2020), the binary pair decreases in separation from 300 AU to 10 AU in only ∼30 radial incursions, at which point it becomes a Keplerian bound pair and its orbital decay is slowed down. In this scenario, orbital decay occurs early in the star-formation process, and circumbinary accretion represents the late stage of binary formation.

4. APPLICATIONS OF CIRCUMBINARY ACCRETION

4.1. Massive Black Hole Binaries and the Final Parsec Problem

In the ΛCDM paradigm of cosmology, MBH encounters are expected to occur as a natural consequence of hierarchical structure growth. If most galaxies host an MBH in their nuclei (Magorrian et al. 1998, Kormendy & Ho 2013), then MBHBs should be an inevitable consequence of galaxy mergers (Begelman et al. 1980). Indeed, the discovery of dual AGNs with kiloparsec separations confirms that galactic mergers can form wide MBH pairs (for a review, see De Rosa et al. 2019). Likewise, because galaxy mergers funnel large amounts of gas toward the center of the merger remnant (e.g., Hopkins et al. 2006), the formation of gaseous CBDs should occur alongside that of MBHBs. It is generally assumed that, if MBHBs form, they evolve toward merger one way or another (for a review, see Colpi 2014). Such mergers are of great importance for low-frequency GW astronomy in the LISA band (Haehnelt 1994, Amaro-Seoane et al. 2017) and the pulsar timing array (PTA) band (Burke-Spolaor et al. 2019).

Following galaxy mergers, dynamical friction by gas/stars and stellar "loss-cone" scatterings would serve to reduce the separations of MBHBs to about one parsec, whereas gravitational radiation would become effective (and make the BHs merge) only if their separations are less than about 0.01 pc (e.g., Begelman et al. 1980, Polnarev & Rees 1994). Binary orbital evolution in the intermediate separation regime is a long-standing problem known as the "final parsec problem" (Milosavljević & Merritt 2003a,b).

CBDs have been posited to be a gas-dynamical solution to this final parsec problem (stellar-dynamical solutions, by contrast, have been thoroughly studied in the literature; e.g., Yu & Tremaine 2002, Vasiliev et al. 2015, Gualandris et al. 2017). In the CBD hypothesis, an MBHB embedded in a viscous accretion disk is forced to migrate inward along with the accretion flow, much like a massive planet embedded in a protoplanetary disk would (Gould & Rix 2000). Most if not all cosmological-scale studies of MBHB coalescence that consider the influence of gas assume CBDs always promote inwardly driven migration (Haiman et al. 2009; Kelley et al. 2017a,b, 2018; Volonteri et al. 2020, 2022). The studies of CBD accretion of recent years put this standard assumption into question, potentially introducing a major caveat to the expected detection rates for LISA (e.g., Sesana et al. 2005) and PTAs (e.g., Sesana et al. 2008).

Despite the encouraging discovery of wide dual AGNs (e.g., Goulding et al. 2019), the direct observation of spatially resolved, subparsec MBHBs will remain all but impossible for the foreseeable future (with the possible exception of very long baseline interferometric observations of nearby galaxies; Burke-Spolaor 2011). Thus, until a direct GW measurement of the inspiral and merger of two MBHs is made, indirect detection methods will be needed to probe the ellusive subparsec regime.

4.1.1. Indirect signatures of ongoing circumbinary accretion onto massive black hole binaries. Spatially resolving MBHBs at subparsec separations is difficult. The most compact, directly imaged MBHB on record is the dual AGNs in the radio galaxy 0402+379, with a projected separation of 7.3 pc (Rodriguez et al. 2006). For more compact sources, photometric and spectroscopic techniques can be used to infer the presence of MBHBs. Circumbinary accretion may prove crucial for upcoming multimessenger efforts to identify such compact MBHBs in the form of periodically varying electromagnetic (EM) counterparts (e.g., Bogdanović et al. 2022, Charisi et al. 2022). The sought-after periodic signals in time-variable AGNs include (*a*) time-variable kinematic offsets of the broad emission lines (Gaskell 1996), (*b*) Doppler-boosted broad-band emission from the circumsecondary accretion disk (D'Orazio et al. 2015), (*c*) periodic self-lensing flares (D'Orazio & Di Stefano 2018, Hu et al. 2020), and (*d*) broadband photometric variability due to pulsed/modulated accretion (e.g., Tang et al. 2018). In practice, the kinematics approach is of limited use at subparsec because of the confusion and truncation of the distinct broad-line regions at these separations (Kelley 2021), making the photometric approach a more viable and data-rich technique (e.g., Charisi et al. 2022). Indeed, systematic searches for periodic signals in the Catalina Real-time Transient Survey (Graham et al. 2015), the Palomar Transient Factory (Charisi et al. 2016), and the Panoramic Survey Telescope and Rapid Response System (Liu et al. 2019b) have revealed hundreds of MBHB candidates. Measuring photometric variability is not exempt from systematic uncertainties (Graham et al. 2015, Liu et al. 2016, Witt et al. 2022) but has the potential of being a powerful multimessenger tool in combination with simultaneous GW detections (Charisi et al. 2022). At subparsec separations, MBHBs emit GWs in the frequencies suitable for PTAs, which are forecast to provide individual binary detections within the next decade (Mingarelli et al. 2017, Kelley et al. 2018). In this regime, the binary orbit is still essentially Newtonian, and the associated GW waveforms are well understood. Likewise, the known photometric variability mechanisms (accretion/boosting/lensing) are all modulated on timescales commensurate with the binary

orbit. Simultaneous GW/photometric detection of these objects would not only conclusively prove their existence but also allow for constraints on the their orbital parameters.

4.1.2. Imprints of circumbinary accretion on massive black hole binary orbits. In addition to detecting circumbinary accretion "in action" in the form of the photometric variability of individual sources, CBD physics can also leave an imprint in the population of MBHBs responsible for the stochastic GW background (GWB; e.g., Zimmerman & Hellings 1980, Thorne 1987, Rajagopal & Romani 1995, Phinney 2001), which is detectable by the method of pulsar timing (Sazhin 1978, Detweiler 1979, Bertotti et al. 1983). The GWB spectrum can be computed from the GWs emitted from MBHB mergers across cosmic scales (Phinney 2001), although the uncertainties in its amplitude and spectral slope depend on the astrophysics of MBHB assembly (Sesana et al. 2008) and on whether or not binary coalescence is delayed, suppressed, or biased toward a specific range in binary mass M_b (e.g., Shannon et al. 2015, Middleton et al. 2018). Furthermore, recent calculations also conclude that the GWB can depend on the eccentricity distribution of the binaries (Kelley et al. 2017b), and on the preferential accretion ratio (Siwek et al. 2020). Consequently, the physics of circumbinary accretion can have a major impact in the GWB.

4.2. Binary Star Formation

The existence of tidally cleared disks (e.g., Dutrey et al. 1994, Jensen & Mathieu 1997, Mathieu et al. 1997, Carr et al. 2001, Ireland & Kraus 2008, Czekala et al. 2021) or rotationally supported structures (Tobin et al. 2016, Maureira et al. 2020) around young stellar binaries, plus the confirmation that such binaries may accrete in a modulated fashion (Basri et al. 1997; Jensen et al. 2007; Muzerolle et al. 2013; Tofflemire et al. 2017a,b, 2019), have underscored the importance of binary–disk interaction in early stellar evolution. These stellar CBDs also contain information about circumbinary planet (CBP) formation (see Section 4.3 below) and can serve as laboratories and proxies for the circumbinary physics taking place in galactic nuclei (Section 4.1).

Tidal truncation and pulsed accretion in young binaries (already discussed in Section 3) are the most straightforward smoking guns for circumbinary accretion. But other important clues of past circumbinary accretion may be found in the evolved population as well. These include binary mass ratios and the overabundance of stellar twins, and migration history of compact and wide binaries.

4.2.1. The over-abundance of stellar twins. Over the past few decades, several studies have consistently shown that stellar binaries exhibit an overabundance of twins (with mass ratio $q_b > 0.95$) (Lucy & Ricco 1979; Tokovinin 2000; Halbwachs et al. 2003; Lucy 2006; Raghavan et al. 2010; Moe & Di Stefano 2013, 2017). This finding is in agreement with some early hydrodynamical simulations that showed that, in binaries accreting from rotating gas, the secondary grew faster that the primary (Bate 2000; but see also Artymowicz 1983, Bonnell & Bastien 1992). Indeed, high-resolution CBD simulations that systematically compute the ratio of accretion rates in circular binaries find that the secondary accretes more than the primary, and the ratio $\dot{M}_2/(\dot{M}_1 + \dot{M}_2)$ decreases monotonically with increasing q_b (see **Figure 11**).

The twin excess was originally reported to be most significant at short orbital periods of $P_b \lesssim 20$ days or $a_b \lesssim 0.4$ AU, (Moe & Di Stefano 2017; see also Tokovinin 2000, Raghavan et al. 2010), which was interpreted as being consistent with the once-held idea that accreting binaries always migrate inward (see discussion in Raghavan et al. 2010). In recent years, however, astrometric measurements (using *Gaia* data) have revealed that the twin excess fraction is roughly constant for projected binary separations between 0.01 au and 10,000 AU (El-Badry et al. 2019).

This finding contradicts the assumption that equal masses and compact orbits are two sides of the same coin. Instead, the large separation of twins may indicate that outward migration due to CBDs has occurred. But even if CBDs promote softer orbits in addition to equal masses, they alone may not produce binary orbits as wide as $\sim 10^4$ AU. El-Badry et al. (2019) conjecture that twins form first with separations of $a_b \lesssim 100$ AU, while accreting from CBDs, and are subsequently widened by dynamical interactions in their parental clusters. The fact that these binaries also tend to be eccentric (Hwang et al. 2022) adds credence to the hypothesis that these orbits have been subject to strong perturbations after gas has dissipated.

4.2.2. Formation of close binaries. In light of the emerging paradigm that binaries accreting from warm disks tend to expand (see Section 3), the origin of 1–10-AU-scale binaries remains a puzzle. Numerical simulations suggest that binary stars initially form with large separations ($\gg 10^2$ AU) (see Offner et al. 2022). The difficulty lies in the impossibility of fragmenting a disk at small separations in which cooling is inefficient (Matzner & Levin 2005, Rafikov 2005, Boley et al. 2006, Whitworth & Stamatellos 2006, Stamatellos & Whitworth 2008, Cossins et al. 2009, Kratter et al. 2010) and in the impossibility of directly fragmenting a core when these are stable against nonaxisymmetric perturbations (and because the size of the first hydrostatic core is already a few astronomical units in size; Bate 1998). Naturally, a significant inward migration would be needed to produce close binaries.

A likely solution to this conundrum is that the required migration takes place at the early (Class 0-I) stage of star formation, when the newly fragmented binaries are still embedded in massive envelopes (see Tokovinin & Moe 2020). As discussed in Section 3.7, some simulations of 3D collapse with embedded binaries do show binary orbital decay at rates faster than the Lindblad torques of the associated CBDs. In some cases, these "binaries" decay because they are not a bound pair initially, and their orbital evolution is dominated by dynamical friction and gas accretion from the envelope.

4.3. Planets Around Binaries

One of the most exciting results in exoplanetary science in recent years was the discovery of CBPs. The Kepler mission has discovered 13 CBPs around 11 eclipsing binaries (e.g., Doyle et al. 2011, Welsh & Orosz 2018, Socia et al. 2020), and the TESS mission has so far (as of Oct. 2022) detected two CBP systems (Kostov et al. 2020, 2021). Most of these are large planets (with radii between $0.3R_J$ and R_J) in a sub-AU, nearly coplanar orbit around the host binary. A handful of CBP systems have been discovered using gravitational microlensing (OGLE-2007-BLG-349; Bennett et al. 2016), and direct imaging (e.g., HD 106906; Bailey et al. 2014, Lagrange et al. 2016, Rodet et al. 2017). In addition, a number of CBP systems have been inferred using eclipse timing variations of binaries (e.g., NN Serpentis; Qian et al. 2009, Beuermann et al. 2010), although the validity of these planets remains uncertain.

Recent studies suggest that the occurrence rate of large, Kepler-like CBPs is comparable with that of similar-mass planets in single-star systems ($\sim$10%; Armstrong et al. 2014, Martin & Triaud 2014, Martin et al. 2019), indicating that planet formation in CBDs is a robust process.

Close-in planetary orbits around a binary are known to be dynamically unstable (e.g., Dvorak et al. 1989, Pilat-Lohinger et al. 2003, Doolin & Blundell 2011). For binaries with $q_b \sim 1$, the critical planetary semimajor axis a_{crit} is about a few times a_b. Holman & Wiegert (1999) provide an approximate expression of a_{crit} based on simulation of circular, coplanar circumbinary particles:

$$a_{crit} = \left(1.6 + 5.1e_b - 2.22e_b^2 + 4.12\mu_2 - 4.27e_b\mu_2 - 5.09\mu_2^2 + 4.61e_b^2\mu_2^2\right) a_b, \qquad 23.$$

where $\mu_2 = M_2/M_b$. A striking feature of the CBPs discovered by *Kepler* is that many of them lie close to the instability boundary (e.g., Kepler-16b has a semimajor axis of $a_p = 1.09a_{crit}$, and Kepler-34b has $a_p = 1.14a_{crit}$). This feature cannot be explained by the selection bias of transit observations (Li et al. 2016). It has been commonly interpreted as evidence for planetary migration, because the circumbinary cavity acts as a "trap" in which migrating planets can be "parked" (e.g., Masset et al. 2006; Pierens & Nelson 2008, 2013; Kley & Haghighipour 2014; Kley et al. 2019; Penzlin et al. 2021; Coleman et al. 2022). The precise stopping location of the planet (for a given binary) depends on various disk parameters (such as viscosity and disk aspect ratio), which affect the intrinsic cavity size, and on the planetary mass—a massive planet opens a gap in the disk and circularizes the inner cavity and, thus, tends to migrate closer to the binary. Current hydrodynamical simulations struggle to reproduce systems such as Kepler-34b, an eccentric ($e_p = 0.18$) planet orbiting very close to an eccentric binary ($e_b = 0.52$), because the central cavity is large and has a significant eccentricity, causing the planet to park too far away (e.g., Pierens & Nelson 2013, Penzlin et al. 2021). The eccentricity of the inner CBD (see Section 3.3) can also leave an imprint on embedded CBPs. In particular, low-mass planets can inherit the eccentricity of the gas disk and precess with it in a state of apsidal corotation (Thun & Kley 2018, Penzlin et al. 2021). Clearly, the close-in CBPs provide clues on the intricate interplays of binary–disk and planet–disk interactions.

In situ formation of CBPs at close-in locations are generally difficult because of the large impact velocities between planetesimals driven by the perturbations on the planetesimal orbits from the binary potential and nonaxisymmetric density features within the CBD. Such large impact velocities lead to corrosive collisions and prevent the buildup of large planetary bodies (Scholl et al. 2007, Marzari et al. 2008, Meschiari 2012, Paardekooper et al. 2012). The motion of planetesimals, however, can depend on the CBD as much as on the central binary. Rafikov (2013) and Silsbee & Rafikov (2015) found that the (secular) planetesimal dynamics is affected by the gravity and gas drag from a precessing eccentric CBD. These effects (for sufficiently massive CBDs) may suppress the excitation from the binary and couple to it resonantly, defining specific regions of the CBD where planetesimals can grow into planets. Gas drag is fundamental in permitting planet formation under external eccentricity perturbations because it can lead to coherent eccentric orbits (Silsbee & Rafikov 2015) and/or coherent "most circular" closed orbits (Pichardo et al. 2005, Lithwick & Wu 2008, Youdin et al. 2012, Bromley & Kenyon 2015). Planetesimals in such orbits would still have low relative velocities, meaning that growth via collisions would not be hampered by the global eccentricity. Overall, these studies suggest that close-in CBPs formed at relatively large distances ($\gtrsim 10a_b$) and move to their current orbits through disk-driven migration.

4.4. Post–Main Sequence Binaries

The final evolution of 0.8–8-$M_\odot$ stars involves a rapid transition from the AGB over the post-AGB phase toward the planetary nebulae stage. Many post-AGB stars are in binary systems (with a main sequence companion). It is now well-established that most post-AGN binaries (with periods from a hundred to a few thousand days) are surrounded by circumbinary gas-dust disks; the observational evidence comes from the disk-like spectral energy distribution of the systems, IR imaging, and CO interferometry that resolves the Keplerian velocity field (e.g., Van Winckel et al. 2009, Van Winckel 2018, Kluska et al. 2022). Many of these binaries also have a bipolar outflow/jet launched from the circumstellar disk around the secondary (main sequence) companion (e.g., Bollen et al. 2021, 2022). The circumstellar disk is likely fed from the CBD, although mass transfer from the post-AGB primary star cannot be ruled out.

The origin of the CBDs around post-AGB binaries is somewhat unclear. These disks are formed as a result of binary interactions during the AGB phase. One possibility is that during

the common-envelope (CE) stage, not all of the envelope is ejected, and a fraction of the mass falls back to the remnant binary in the form of a CBD (e.g., Sandquist et al. 1998, Kashi & Soker 2011). One issue with this scenario is that CE evolution is expected to produce systems with periods ranging from hours to hundreds of days, and yet no CBD has been observed around systems with periods less than 100 days. Another possibility is mass loss through the outer Lagrangian point L_2 associated with the mass transfer or wind of the AGB star (e.g., Shu et al. 1979, de Val-Borro et al. 2009, Pejcha et al. 2016), although it is unclear if stable (and long-lasting) CBD can be produced in this way.

CBDs may produce some dynamical effects on the post-AGB binaries or other evolved binaries. Many post-AGB binaries with periods of a hundred to a few thousands days are observed to have significant eccentricities (up to $e_{\rm b} \simeq 0.6$; Van Winckel 2018). This is surprising because such binaries are supposed to have circularized during the AGB phase. Dermine et al. (2013) suggested that the eccentricities of the post-AGB binaries could be excited as a result of their gravitational interaction with the CBD. Antoniadis (2014) suggested that a similar effect could explain the eccentricities of some binary millisecond pulsars with the white dwarf companions. The eccentricity-growth mechanism can be easily understood from gravitational binary–CBD interaction (e.g., Goldreich & Tremaine 1980, Lubow & Artymowicz 1996). From Section 2, we know that the binary loses angular momentum and energy through the OLR associated with the (mn) potential component at the rates $\mathrm{d}J_{\rm b}/\mathrm{d}t = -T_{mn}$ and $\mathrm{d}E_{\rm b}/\mathrm{d}t = -\omega_{mn}T_{mn}$. These imply that the binary eccentricity evolves at the rate of

$$\dot{e}_{\rm b} = \frac{(1-e_{\rm b}^2)^{3/2}T_{mn}}{e_{\rm b}J_{\rm b}}\left[(1-e_{\rm b}^2)^{1/2} - \frac{\omega_{mn}}{\Omega_{\rm b}}\right]. \qquad 24.$$

For small but finite $e_{\rm b}$, the $m = 2$ and $n = -1$ potential component has $\omega_{mn} = \Omega_{\rm b}/3$, and $T_{mn} \propto e_{\rm b}^2$, leading to $\dot{e}_{\rm b}/e_{\rm b} > 0$.

It is important to note that Equation 24 relies on pure gravitational interaction between the binary and the CBD. This could apply in the "transient" stage before gas accretion onto the binary sets in [see, for example, the simulation of accretion from a finite-sized CBD by Muñoz et al. (2020)]. However, as discussed in Section 3.4, once the accretion starts (typically within a viscous time of the inner disk) and the system settles into a quasi-steady state, the secular evolution of the binary can be quite different from that predicted by the pure gravitational effect. In addition, when applying Equation 24 to post-AGB binaries, it is not clear that the CBD has a sufficient mass to change the binary eccentricity in an appreciable way even if the accretion effect is ignored (Rafikov 2016). Obviously, more works are needed to understand the origin of the peculiar eccentricities of the post-MS binaries.

5. MISALIGNED DISKS

In the previous sections, we have focused on aligned disks, i.e., disks that are coplanar with their central binaries. Such alignments may not be realized in many situations. For example, in the current theory of star formation, supersonic turbulence in molecular clouds leads to the creation of clumps, which then condense and fragment into stars and binaries (e.g., McKee & Ostriker 2007). The gas that falls on to the central protostellar core/binary and assembles on to the disk at different times may rotate in different directions (Bate et al. 2003, 2010; Offner et al. 2010; Tsukamoto & Machida 2013; Fielding et al. 2015; Takaishi et al. 2020). In this scenario, it is reasonable to expect a newly formed binary to be surrounded by a highly misaligned CBD, which forms as a result of continued gas accretion. Similar chaotic accretion may also occur in the formation of MBHs (e.g., King & Pringle 2006). In particular, MBHBs at the centers of galaxies may experience accretion

of successive low-mass gas "clouds" with uncorrelated angular momenta, which naturally lead to misaligned CBDs.

Observationally, most CBDs around young stellar binaries are found to be aligned with their host binary orbital planes (Czekala et al. 2019). For example, the gas-rich CBDs AK Sco (Czekala et al. 2015) and DQ Tau (Czekala et al. 2016) and the debris disks α CrB and β Tri (Kennedy et al. 2012b) all have mutual disc–binary inclinations less than a few degrees. However, there are some notable exceptions. For example, the pre-MS binary KH 15D possesses a low inclination (10–20 deg) precessing circumbinary ring or disk (Chiang & Murray-Clay 2004, Winn et al. 2004, Capelo et al. 2012, Poon et al. 2021) (for two similar systems discovered by ZTF, see Zhu et al. 2022). The disks (circumbinary and two circumstellar) in the system IRS 43 are highly misaligned ($\sim$60 deg) with each other and with the binary (Brinch et al. 2016). The gaseous CBD around the eccentric binary HD 98800B is nearly polar (with a misalignment angle of $\sim$90 deg; Kennedy et al. 2019). The 6–10-Gyr-old eccentric binary 99 Herculis has a nearly polar ($\sim$87 deg) debris ring around it (Kennedy et al. 2012a). The young ($\sim$1 Myr) hierarchical triple star system GW Ori possesses a misaligned circumtriple disk with three broken dusty rings (Bi et al. 2020, Kraus et al. 2020).

5.1. Disk Warping, Breaking, and Alignment

Consider a CBD surrounding a circular binary (with total mass $m_{\rm b}$, reduced mass $\mu_{\rm b}$, semimajor axis $a_{\rm b}$, and eccentricity $e_{\rm b} = 0$). The orientation of the disk at radius r (from the center of mass of the binary) is specified by the unit normal vector $\hat{\boldsymbol{l}}(r,t)$. Averaging over the binary orbital period and the disk azimuthal direction, the binary imposes a torque per unit mass on the disk element at radius r given, to the leading order in $a_{\rm b}/r$, by

$$\boldsymbol{T}_{\rm b} = -r^2\Omega\,\omega_{\rm proc}(\hat{\boldsymbol{l}}_{\rm b}\cdot\hat{\boldsymbol{l}})(\hat{\boldsymbol{l}}_{\rm b}\times\hat{\boldsymbol{l}}), \tag{25.}$$

where $\Omega = (GM_{\rm b}/r^3)^{1/2}$ is the orbital frequency at radius r, $\hat{\boldsymbol{l}}_{\rm b}$ is the unit vector along the binary angular momentum axis, and

$$\omega_{\rm prec} = \frac{3\mu_{\rm b}}{4M_{\rm b}}\left(\frac{a_{\rm b}}{r}\right)^2\Omega \tag{26.}$$

characterizes the (nodal) precession rate of the disk mass element around the binary axis. Because $\omega_{\rm prec}$ depends strongly on r, the disk would lose coherence if different parts of the disk did not "communicate" with each other. In reality, the combination of differential precession and internal fluid stresses can give rise to a coherently warped/twisted disk.

Theoretical studies of warped disks (Papaloizou & Pringle 1983, Papaloizou & Lin 1995) have shown that there are two dynamical regimes for the linear propagation of warps in an accretion disk. For high-viscosity disks with $\alpha \gtrsim h \equiv H/r$ (where H is the half-thickness of the disk and α is the Shakura–Sunyaev parameter such that the viscosity is $\nu = \alpha H^2\Omega$), the warp is communicated via angular momentum advection by the oscillatory internal flow whose amplitude is determined by the viscosity and satisfies a diffusion-type equation. The corresponding diffusion coefficient ν_2 measures the r–z viscous stress and can differ from the usual viscosity ν (which measures the r–ϕ stress).[2] Ogilvie (1999) has developed a fully nonlinear theory of diffusive warps that is in agreement with 3D numerical simulations (Lodato & Price 2010). In such a high-viscosity regime,

[2]For Keplerian disks, resonance between the epicyclic frequency and orbital frequency leads to $\nu_2/\nu = 1/(2\alpha^2) \gg 1$. However, the resonance can be easily "detuned" by small non-Keplerian effects such as general relativity or quadrupole potential from the binary (see Ogilvie 1999).

we expect that an inclined CBD at large radii will transition to alignment with the binary at small radii, with the characteristic transition radius ("warp radius") $r_{\rm warp}$ determined by $\omega_{\rm prec}(r_{\rm warp}) \simeq \nu_2/r_{\rm warp}^2$, giving

$$\frac{r_{\rm warp}}{a_{\rm b}} \simeq 14 \left(\frac{4\mu_{\rm b}}{M_{\rm b}} \frac{\nu}{\nu_2} \frac{0.1}{\alpha} \right)^{1/2} \frac{0.1}{h}. \tag{27.}$$

(This warp transition behavior is similar to the Bardeen–Petterson effect of accretion disks around spinning BHs; e.g., Bardeen & Petterson 1975, Kumar & Pringle 1985, Scheuer & Feiler 1996).

Depending on the initial condition, a misaligned viscous CBD may be susceptible to tearing (i.e., breaking up into two or more disconnected "rings") if the steady warped state cannot be attained. Such disk tearing was observed in the SPH simulations of Nixon et al. (2013) when the CBD is initiated with a sufficiently large inclination angle θ with respect to the binary (see also Nealon et al. 2020). The disk breaking radius can be estimated by comparing the viscous warp torque (per unit mass) $(\nu_2/r^2)r^2\Omega$ to the precessional torque from the binary, $|T_{\rm b}| \sim \omega_{\rm prec} r^2 \Omega |\sin 2\theta|$, giving

$$r_{\rm break} \simeq r_{\rm warp} |\sin 2\theta|^{1/2}. \tag{28.}$$

Disk breaking requires sufficiently large θ, for which $r_{\rm break} \sim r_{\rm warp}$. If the initial θ is small such that $r_{\rm break}$ lies inside the inner radius of the CBD, disk breaking would not occur, and we expect the disk to evolve into the steady warped state, with a smooth transition between alignment (with the binary) at small radii and misalignment at large radii.

For low-viscosity disks with $\alpha \lesssim h$, a low-amplitude warp propagates as a bending wave at about half the sound speed, $c_{\rm s}/2$, provided that the disk is sufficiently Keplerian (i.e., the apsidal precession and nodal precession rates are less than $h\Omega$) (Lubow & Ogilvie 2000; see also Lubow et al. 2002, Ogilvie 2006). Protoplanetary disks around young binary stars (with $\alpha \sim 10^{-4}$–10^{-2}, $h \gtrsim 0.05$, and $r/a_{\rm b} \gtrsim$ a few) generally satisfy these conditions (Foucart & Lai 2013). The nonlinear behavior of low-viscosity warped disks is complicated and poorly understood owing to the resonant excitation of vertical "breathing" motions (Fairbairn & Ogilvie 2021) and a parametric instability associated with the inertial waves (Gammie et al. 2000, Ogilvie & Latter 2013, Paardekooper & Ogilvie 2019, Deng et al. 2021, Deng & Ogilvie 2022).

Because of the efficient communication of warps by the bending waves, an inclined protostellar disk around a binary is approximately flat—this is the case provided that the bending wave crossing time $2r/c_{\rm s}$ is shorter than the characteristic precession time $\omega_{\rm prec}^{-1}$, which is a condition that is well satisfied everywhere in the disk except the innermost region (Zanazzi & Lai 2018a). The interplay between the small (nonzero) disk twist/warp and viscous dissipation drives the long-term evolution of the disk inclination. Foucart & Lai (2013, 2014) studied the warp and the dissipative torque that drives the inclination evolution of a CBD around a circular binary. Foucart & Lai (2013) considered an infinite disk and included the effect of accretion onto the binary, whereas Foucart & Lai (2014) considered a more realistic disk of finite size and angular momentum, which can precess coherently around the binary. They showed that under typical protoplanetary conditions, both viscous torque associated with disk warp/twist and accretion torque tend to damp the mutual disk–binary inclination on timescales much shorter than the disk lifetime (a few million years). In contrast, a circumstellar disk inside a binary can maintain large misalignment with respect to the binary orbital plane over its entire lifetime (Lubow & Ogilvie 2000, Foucart & Lai 2014). Qualitatively, the key difference between CBDs and circumstellar disks is that in the former (latter), the binary torque is exerted at the inner (outer) region of the disk, which contains a small (larger) amount of angular momentum, leading to relatively large (small) warp and, thus, faster (slower) viscous damping. Overall, these results are consistent with the observations that most CBDs are

nearly coplanar with their host binaries (Czekala et al. 2019), whereas circumstellar disks within young stellar binaries are often misaligned (e.g., Jensen & Akeson 2014, Ichikawa et al. 2021).

5.2. Polar Alignment of Disks Around Eccentric Binaries

Although disks around circular binaries tend to evolve toward alignment, recent works suggested that other outcomes may be possible for disks around eccentric binaries. Aly et al. (2015) carried out SPH simulations of disks around eccentric MBHBs (which typically lie in the "viscous" regime of disk warps, with $\alpha \gtrsim h$), and showed that the disk may be driven into polar alignment (i.e., the disk plane is perpendicular to the binary plane). Martin & Lubow (2017) found numerically that a circumbinary protoplanetary disk (typically in the bending-wave regime, with $\alpha \lesssim h$) inclined to an eccentric ($e_{\rm b} = 0.5$) binary by 60 deg will evolve to a polar configuration. This dynamical outcome arises from the combined influences of the gravitational torque on the disk from the eccentric binary and viscous torque from disk warping.

To understand the possibility of polar alignment, it is useful to consider the secular dynamics of a circular test particle around an eccentric binary (e.g., Farago & Laskar 2010, Li et al. 2014).

$$\boldsymbol{T}_{\rm b} = -r^2 \Omega\, \omega_{\rm prec} \big[(1-e_{\rm b}^2)(\hat{\boldsymbol{l}} \cdot \hat{\boldsymbol{l}}_{\rm b}) \hat{\boldsymbol{l}}_{\rm b} \times \hat{\boldsymbol{l}} - 5 (\hat{\boldsymbol{l}} \cdot \boldsymbol{e}_{\rm b}) \boldsymbol{e}_{\rm b} \times \hat{\boldsymbol{l}} \big], \tag{29.}$$

where $\boldsymbol{e}_{\rm b}$ is the binary eccentricity vector. In the absence of hydrodynamical forces, the time evolution of the test particle's orbital angular momentum vector $\hat{\boldsymbol{l}}$ is governed by $\mathrm{d}\hat{\boldsymbol{l}}/\mathrm{d}t = \boldsymbol{T}_{\rm b}/(r^2\Omega)$. It is clear that the evolution of $\hat{\boldsymbol{l}}$ has four possible fixed points (where $\mathrm{d}\hat{\boldsymbol{l}}/\mathrm{d}t = 0$): $\hat{\boldsymbol{l}} = \pm \hat{\boldsymbol{l}}_{\rm b}$ and $\hat{\boldsymbol{l}} = \pm \boldsymbol{e}_{\rm b}/e_{\rm b}$. To examine the stability of the fixed points, it is useful to analyze the trajectory of $\hat{\boldsymbol{l}}(t)$ using the "energy" curves. The equation of motion for $\hat{\boldsymbol{l}}(t)$ admits an integral of motion,

$$\Lambda = (1-e_{\rm b}^2)(\hat{\boldsymbol{l}} \cdot \hat{\boldsymbol{l}}_{\rm b})^2 - 5(\hat{\boldsymbol{l}} \cdot \boldsymbol{e}_{\rm b})^2, \tag{30.}$$

which is simply related to the quadrupole interaction energy (double-averaged over the binary and test-particle orbits) by (e.g., Tremaine et al. 2009, Liu et al. 2015)

$$\Phi_{\rm quad} = \frac{G\mu_{\rm b} a_{\rm b}^2}{8r^3} (1 - 6e_{\rm b}^2 - 3\Lambda). \tag{31.}$$

Figure 14 shows the test particle trajectories (constant−Λ curves) in the I–Ω (**Figure 14*a***) and I_e–Ω_e (**Figure 14*b***) planes for $e_{\rm b} = 0.3$. The critical separatrix $\Lambda = 0$ is displayed in both plots. When $\Lambda > 0$, $\hat{\boldsymbol{l}}$ precesses around $\hat{\boldsymbol{l}}_{\rm b}$ with $I \sim$ constant and Ω circulating the full range (0–360 deg). When $\Lambda < 0$, $\hat{\boldsymbol{l}}$ precesses around $\boldsymbol{e}_{\rm b}$ with $I_e \sim$ constant and Ω_e circulating the full range (0–360 deg). Thus, the test particle angular momentum axis $\hat{\boldsymbol{l}}$ transitions from precession around $\hat{\boldsymbol{l}}_{\rm b}$ for $\Lambda > 0$ to precession around $\boldsymbol{e}_{\rm b}$ for $\Lambda < 0$. A necessary condition for $\hat{\boldsymbol{l}}$ to precess around $\boldsymbol{e}_{\rm b}$ is $I_{\rm crit} < I < 180\ {\rm deg} - I_{\rm crit}$, where

$$I_{\rm crit} = \cos^{-1} \sqrt{\frac{5e_{\rm b}^2}{1+4e_{\rm b}^2}} = \tan^{-1} \sqrt{\frac{1-e_{\rm b}^2}{5e_{\rm b}^2}}. \tag{32.}$$

Zanazzi & Lai (2018b) carried out a detailed theoretical analysis of the dynamics of inclined, warped disks around eccentric binaries and their long-term evolution driven by viscous torques (see also Lubow & Martin 2018). For disks with $H/r \gtrsim \alpha$ (as appropriate for protoplanetary disks), bending wave propagation effectively couples different regions of the disk, making it precess as a quasi-rigid body. Zanazzi & Lai showed explicitly that the dissipative torque (associated with disk warp/twist) tends to drive the disk to one of two states, depending on the initial sign of Λ: For $\Lambda > 0$, the disk angular momentum axis $\hat{\boldsymbol{l}}_{\rm d}$ aligns (or antialigns) with the binary orbital angular momentum vector $\hat{\boldsymbol{l}}_{\rm b}$; for $\Lambda < 0$, $\hat{\boldsymbol{l}}_{\rm d}$ aligns with the binary eccentricity vector (polar alignment). They also showed that when the disk has a nonnegligible angular momentum compared to the

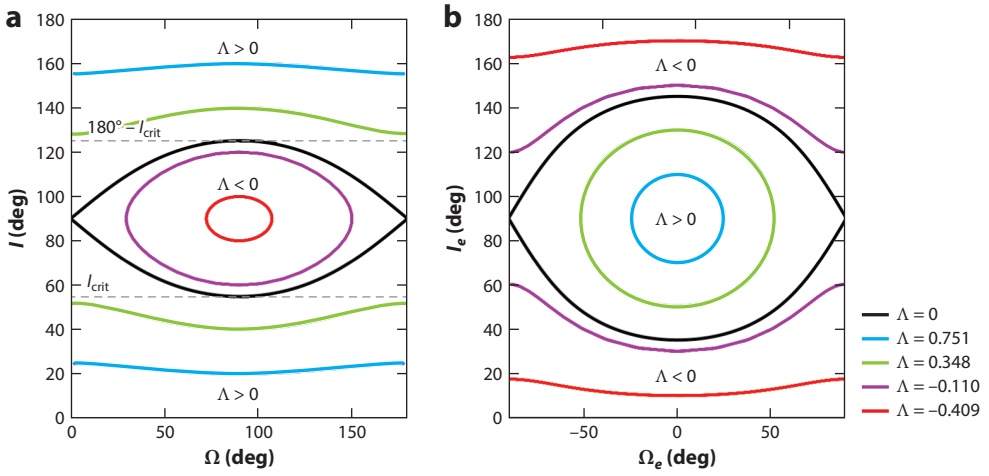

Figure 14

Test particle trajectories around an eccentric binary in the $I - \Omega$ and $I_e - \Omega_e$ planes, with the binary eccentricity $e_b = 0.3$. The inclination angles I (between $\hat{\boldsymbol{l}}$ and $\hat{\boldsymbol{l}}_b$) and I_e (between $\hat{\boldsymbol{l}}$ and $\boldsymbol{e}_b$), and the nodal angles Ω and Ω_e (not to be confused with the angular frequency) are defined by $\hat{\boldsymbol{l}} = (\sin I \sin\Omega, -\sin I \cos\Omega, \cos I) = (\cos I_e, \sin I_e \sin\Omega_e, \sin I_e \cos\Omega_e)$ in the Cartesian coordinate system, where $\hat{\boldsymbol{l}}_b = \hat{\boldsymbol{z}}$ and $\boldsymbol{e}_b = e_b\hat{\boldsymbol{x}}$. When $\Lambda > 0$, $\hat{\boldsymbol{l}}$ precesses around $\hat{\boldsymbol{l}}_b$, with $I \sim$ constant and Ω circulating its full range of values (0 deg–360 deg). When $\Lambda < 0$, $\hat{\boldsymbol{l}}$ precesses around $\boldsymbol{e}_b$, with $I_e \sim$ constant and Ω_e circulating its full range of values (−180 deg–180 deg). Only Ω and Ω_e in the range of [0 deg, 180 deg] and [−90 deg, 90 deg] are shown. Figure adapted from Zanazzi & Lai (2018b).

binary, the system's fixed points are modified and the disk may then evolve to a state of near polar alignment, with the inclination somewhat less than 90 deg (see also Martin & Lubow 2019). Note that Λ depends on both I (the binary–disk inclination) and Ω (the longitude of ascending node of the disk). Thus for a given e_b, the direction of inclination evolution depends not only on the initial $I(0)$ but also on the initial $\Omega(0)$. The timescale of evolution of the disk–binary inclination angle is approximately given by (assuming the disk surface density profile $\Sigma \propto 1/r$)

$$\tau_b \sim 10^4 \left(\frac{0.01}{\alpha}\right)\left(\frac{h}{0.1}\right)^2\left(\frac{r_{in}}{2a_b}\right)^4\left(\frac{M_b}{4\mu_b}\right)^2\left(\frac{2\,M_\odot}{M_b}\right)^{1/2}\left(\frac{r_{out}}{100\,\mathrm{AU}}\right)^{3/2}\mathrm{year}, \qquad 33.$$

where r_{in} and r_{out} are the inner and outer radii of the disk. Thus τ_b is generally less than a few million years of the lifetime of protoplanetary disks. This suggests that highly inclined disks may exist around eccentric binaries.

This theoretical expectation was recently confirmed by the observation of the young (∼10 Myr) protoplanetary system HD 98800. Using Atacama Large Millimeter/submillimeter Array (ALMA) observations of dust and CO emissions, Kennedy et al. (2019) showed that the inner binary BaBb (with $a_b \simeq 1$ AU, $e_b = 0.785$) in the system (which is a "2+2" hierarchical quadruple system with two inner binaries orbiting each other with a semimajor axis of 54 AU) is surrounded by a CBD in a polar-aligned configuration. The old circumbinary debris disk nearly perpendicular to the orbital plane of the binary 99 Herculis (Kennedy et al. 2012a) may also have gone through such polar-alignment processes early in its lifetime when the gas was present (e.g., Smallwood et al. 2020).

Figure 15 (from Czekala et al. 2019) shows the inclinations of *Kepler* CBPs and circumbinary protoplanetary and debris disks as a function of binary orbital period, semimajor axis, and

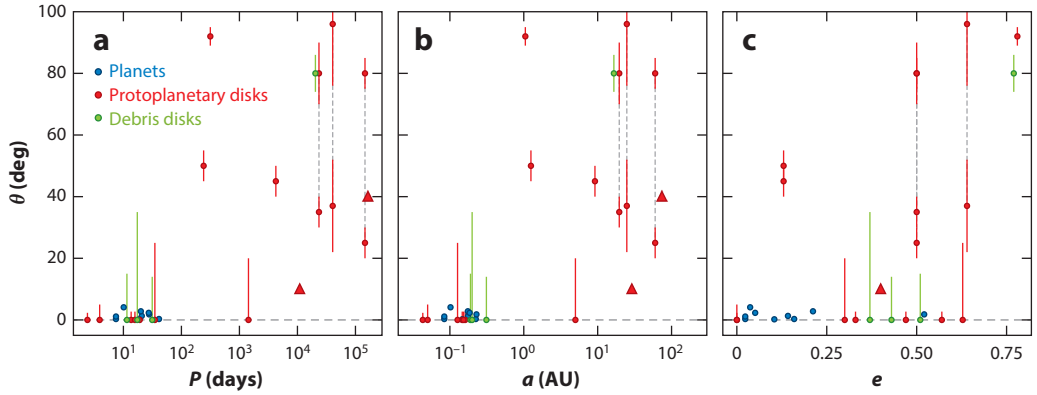

Figure 15

(*a*) The mutual inclinations of *Kepler* circumbinary planets and all circumbinary protoplanetary and debris disks, as a function of binary orbital period. The triangles represent the lower limits on θ for R CrA and IRS 43. (*b*) Mutual inclination as a function of semimajor axis. (*c*) Mutual inclination as a function of binary eccentricity. Note that the binary eccentricity is unknown for IRS 43, and so it is not plotted in the eccentricity panel. The two points at $e = 0.13$ correspond to GW Ori A-B and AB-C, which collectively host a circumternary protoplanetary disk. Long-period, eccentric binaries are more likely to host circumbinary disks with significant mutual inclinations. Figure adapted with permission from Czekala et al. (2019); copyright 2019 AAS.

eccentricity. A clear trend emerges: All CBDs orbiting binaries with a period of less than 30 days (semimajor axis less than 0.4 AU) and/or eccentricity less than 0.2 are consistent with being coplanar, whereas disks orbiting a longer period and/or more eccentric binaries exhibit a wide range of mutual inclinations, from coplanar to polar. The origin of this "critical" orbital period is unclear. But the trend is consistent with the general idea that stellar binaries form/fragment at large separations and migrate inward to small separations in massive disks/envelopes, during which the binary and disk become aligned (see Section 4.2).

The near coplanarity of CBDs around short-period binaries implies that planets formed in such disks should be similarly coplanar. This is consistent with the finding that *Kepler* CBPs, orbiting binaries with $P_b < 40$ days, have small mutual inclinations, and indicates that the planet occurrence rate around such binaries is similar to that for single stars (see also Armstrong et al. 2014, Li et al. 2016, Martin et al. 2019). Beyond $P_b > 40$ days, however, the existence of misaligned CBDs suggests that CBPs around eccentric binaries may be found to have a broad distribution of mutual inclinations, with a possible concentration of polar-aligned systems.

6. BINARIES EMBEDDED IN "BIG" DISKS

A special type of "circumbinary accretion" has gained significant interest in recent years. This concerns stellar binaries embedded in AGN disks around SMBHs.

The detection of GWs from the merging binary BHs by the LIGO/Virgo collaboration (LIGO Sci. Collab. et al. 2021) has motivated many theoretical studies of the formation channels of the BH binaries. In addition to the isolated binary evolution channel (e.g., Lipunov et al. 1997, Belczynski et al. 2016), there are several flavors of dynamical channels, including strong gravitational scatterings in dense star clusters (e.g., Portegies Zwart & McMillan 2000, Kremer et al. 2019), more gentle "tertiary-induced mergers" (often via the Lidov–Kozai mechanism) that take place either in stellar triple/quadruple systems (e.g., Silsbee & Tremaine 2017; Liu & Lai 2018, 2019) or in nuclear clusters dominated by a central SMBH (e.g., Antonini & Perets 2012, Liu et al. 2019a, Liu & Lai 2021), and (hydro)dynamical interactions of binaries in AGN disks (e.g., Bartos et al. 2017, Stone et al. 2017, McKernan et al. 2018, Tagawa et al. 2020). It has also been

suggested that intermediate-mass BHs (IMBHs) may be formed efficiently in AGN disks via accretions or mergers of stars and compact objects (e.g., McKernan et al. 2012, 2014). If these IMBHs are themselves members of binaries, they could be susceptible to "evection resonances" driven by the SMBH's tidal field (Muñoz et al. 2022), which could then accelerate their GW-driven inspiral and produce an eccentric waveform (see also Bhaskar et al. 2022).

In the AGN disk scenario, an important question concerns how single stellar-mass BHs can be captured into bound binaries and merge. J. Li et al. (2022) showed that when the gas effect is negligible, two BHs in tightly packed orbits around an SMBH become bound to each other in rare, very close encounters due to GW emission, leading to highly eccentric BH mergers in the LIGO band. At sufficiently high gas densities, the gas drags on the BHs can facilitate the capture process (e.g., Tagawa et al. 2020, J. Li et al. 2023).

Once a bound BH binary forms in the AGN disk, an important question concerns how the binary evolves in the presence of the surrounding gas. It is tempting to consider this as a "circumbinary accretion" problem (e.g., Stone et al. 2017), with the background AGN disk feeding gas onto the CBD around the binary. For example, one might use the modified Bondi–Hoyle–Lyttleton accretion formula (e.g., Edgar 2004) to estimate the mass supply rate from the background AGN disk (with gas density $\rho_{\rm bg}$ and sound speed $c_{\rm s,bg}$) onto the binary, $\dot{m}_{\rm b} \sim \pi \rho_{\rm bg} v_{\rm eff} r_{\rm acc} \min(r_{\rm acc}, H)$, where H is the disk scale-height and $r_{\rm acc}$ is the accretion radius $r_{\rm acc} \sim G m_{\rm b}/v_{\rm eff}^2$, with $v_{\rm eff}^2 \sim c_{\rm s,bg}^2 + v_{\rm H}^2$ (the second term accounts for the "Hill velocity," the velocity shear across the Hill radius). However, such an estimate could be quite misleading as the strong velocity shear and flow angular momentum can significantly reduce the accretion rate compared to the Bondi–Hoyle–Lyttleton estimate (Li & Lai 2022). In fact, even when the binary is replaced by a single object, the accretion rate can be much smaller than the Bondi–Hoyle–Lyttleton estimate because of the strong upstream velocity shear. Numerical simulations show that the accretion rate generally depends on the physical size of the accretor, indicating that the physics near the accretor can strongly influence the accretion flow (see Xu & Stone 2019). Thus, it is not clear that the results from circumbinary accretion (Section 3) can be directly adapted and applied to the problem of binaries embedded in big disks.

The hydrodynamical evolution of binaries in AGN disks has been studied numerically by a handful of works so far. Baruteau et al. (2011) carried out global simulations in 2D isothermal disks and found that a massive (gap-opening) prograde, equal-mass binary is hardened by dynamical friction from the lagging spiral tails trailing each binary component inside the Hill radius. Li et al. (2021) used a similar global setup and found that adequately resolved CSD regions in fact lead to expanding binaries. Y.P. Li et al. (2022) further found that temperature structure of the CSDs plays an important role in the evolution of the binary.

Resolving CSDs around each binary component is therefore important but is computationally demanding in global disk simulations. A useful approach is to use a corotating local disk ("shearing-box") model, where the global cylindrical geometry of the disk is mapped onto local Cartesian coordinates centered at the binary's center of mass, which rotates around the SMBH. This is the approach adopted by Li & Lai (2023, 2022) and Dempsey et al. (2022). Note that although there are multiple length scales and velocity scales associated with the problem, only a few dimensionless ratios are important. For example, the relevant length scales include the following:

- Binary semimajor axis $a_{\rm b}$;
- Hill radius $R_{\rm H} \equiv R(M_{\rm b}/M)^{1/3} \equiv Rq^{1/3}$, where $M_{\rm b}$ is the total mass of the binary, M is the mass of the SMBH, and R is the orbital radius of the binary around the SMBH (note that this definition of Hill radius differs from the standard one $R'_{\rm H} = R_{\rm H}/3^{1/3}$);
- Bondi radius $R_{\rm B} = GM_{\rm b}/c_{\rm s,bg}^2$, where $c_{\rm s,bg}$ is the sound speed of the background gas (far from the binary);
- Scale height of the background disk $H = c_{\rm s,bg}/\Omega_{\rm K}$, with $\Omega_K = (GM/R^3)^{1/2}$.

However, their ratios depend on only two dimensionless parameters:

$$\frac{R_{\rm H}}{H} = \left(\frac{R_{\rm B}}{H}\right)^{1/3} = \left(\frac{q}{h^3}\right)^{1/3}, \tag{34.}$$

$$\frac{R_{\rm H}}{a_{\rm b}} = \lambda. \tag{35.}$$

Similarly, the relevant velocity scales are $c_{\rm s,bg}$, $v_{\rm b} = (GM_{\rm b}/a_{\rm b})^{1/2}$, the velocity shear across the binary $V_{\rm s} = (3/2)\Omega_{\rm K} a_{\rm b}$, and $|\Delta V_{\rm K}| \sim h^2 V_{\rm K}$ (the deviation of the background gas velocity around the SMBH from the Keplerian velocity). The first three are related by the same dimensionless parameters:

$$\frac{v_{\rm b}}{c_{\rm s,\infty}} = \lambda^{1/2}\left(\frac{q}{h^3}\right)^{1/3}, \tag{36.}$$

$$\frac{V_{\rm s}}{c_{\rm s,\infty}} = \frac{3}{2\lambda}\left(\frac{q}{h^3}\right)^{1/3}. \tag{37.}$$

For thin discs ($h \ll 1$), $|\Delta V_{\rm K}|$ is very subsonic ($|\Delta V_{\rm K}|/c_{\rm s,bg} \sim h \ll 1$) and is typically much smaller than $V_{\rm s}$. Therefore, the flow dynamics and the binary orbital evolution, when appropriately scaled, depend on various physical quantities only through two dimensionless parameters: $q/h^3 = (R_{\rm H}/H)^3$ and λ (in addition to other obvious parameters such as the binary eccentricity and mass ratio). Note that the parameter $q/(3h^3)$ is the ratio of the binary mass $M_{\rm b}$ to the so-called thermal mass, $3h^3 M$. When $R_{\rm H}/H \gtrsim 1$ (which also implies $R_{\rm B} \gtrsim R_{\rm H}$), the flow onto the Hill sphere is quasi-2D, and we expect a CSD to form around each binary component; 2D shearing-sheet simulations are appropriate in this regime. When $R_{\rm H}/H \lesssim 1$, vertical flows onto the Hill sphere are important, and 3D simulations are needed to accurately capture the flow structure (Dempsey et al. 2022). Current models of AGN disks (Sirko & Goodman 2003, Thompson et al. 2005) contain regions with a wide range of $R_{\rm H}/H$ ratio (for typical $M_{\rm b}/M$), from $\lesssim 1$ to $\gg 1$ (see Dempsey et al. 2022, their figure 1). The dynamical stability of the binary requires $\lambda \gtrsim 2$; even for $\lambda \gg 1$, the flow structure still depends on $R_{\rm H}/H$ and can be quite different from that around isolated binaries.

Figure 16 illustrates the flow structure of an equal-mass circular binary embedded in the AGN disk, from the 2D shearing-box simulation of Li & Lai (2022) with $\lambda = 5$, $q/h^3 = 1$, and the gas satisfying the γ-law EOS ($\gamma = 1.6$). Grand spirals originating from the circumbinary flows extend to large distances along the shear flow directions; they can be considered as half bow shocks of the binary accretion with upstream flow gradients due to the shear. Some of these features are also found in the global simulations of Baruteau et al. (2011) and Li et al. (2021). There are also horseshoe flows and the inner/outer shear flows around the binary. Such flow structures are similar to those observed in previous studies of a single accretor (e.g., Fung et al. 2015, Zhu et al. 2016, Kuwahara et al. 2019, Bailey et al. 2021). Due to the fast orbital velocity $v_{\rm b}$, the flow close to the binary is much more dynamic. Both CSDs contain two spiral shocks that drive accretion throughout the disk. Each CSD is then encompassed and attached by a small half bow shock, the tail of which is slingshot away along each grand spiral once per binary orbital period; the propagation of such waves is visible in **Figure 16**. More examples of the flow properties (which depend on $\lambda, q/h^3, \gamma, M_1/M_2$, and $e_{\rm b}$) are discussed by Li & Lai (2023, 2022) and Dempsey et al. (2022; these authors considered 3D simulations with an isothermal EOS). Overall, the flow structure is qualitatively different from that of "circumbinary accretion" discussed in Section 3.

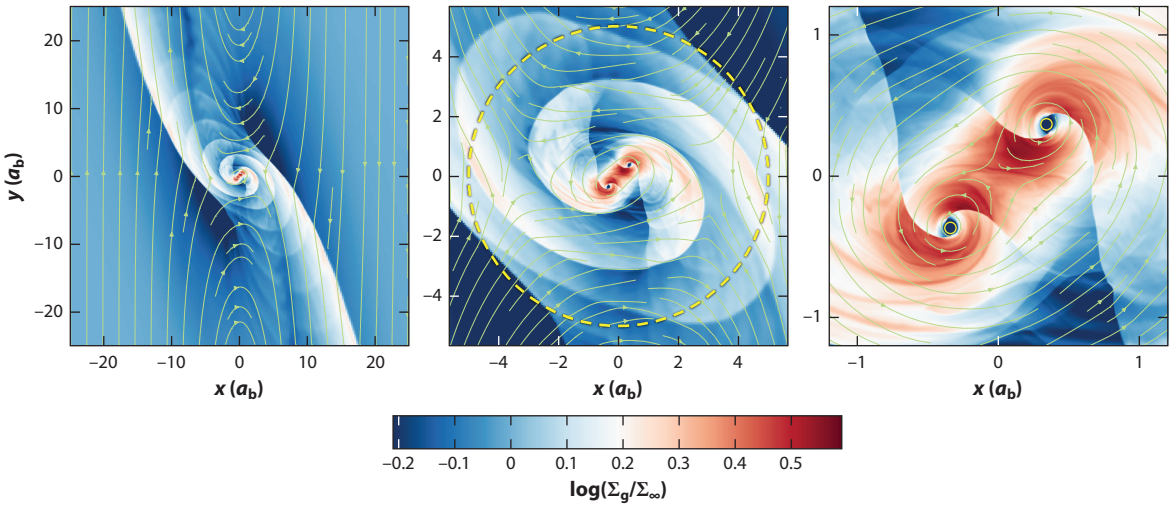

Figure 16

A snapshot of the flow property around an equal-mass, circular binary embedded in a "big" (AGN) disk, where the mesh is refined progressively toward the binary (*zooming in* from *left* to *right*). The parameters are $\lambda = R_H/a_b = 5$, $q/h^3 = 1$ and $\gamma = 1.6$. The shearing-box frame is centered at the center of mass of the binary, and the supermassive black hole is to the left. The background flow (far from the binary) in the shearing box frame is given by $\boldsymbol{V}_w = \boldsymbol{V}_{sh} + \Delta\boldsymbol{V}_K = -(3/2)\Omega_K x\hat{\boldsymbol{y}} + \Delta V_K\hat{\boldsymbol{y}}$, where $\boldsymbol{V}_{sh}(x)$ denotes the Keplerian shear and $\boldsymbol{\Delta V}_K$ is the deviation from Keplerian velocity, with $\Delta V_K \sim -h^2 V_K$. The color specifies the gas surface density (with $\Sigma_\infty = \Sigma_{bg}$ being the background disk density far from the binary). The green streamlines show the detailed flow structure, and the yellow dashed circle in the middle panel with a radius of R_H denotes the Hill radius of the binary. Figure adapted with permission from Li & Lai (2022, the left column of their figure 3); copyright 2022 AAS.

Li & Lai (2023, 2022) have used a suite of high-resolution 2D shearing-box simulations of binaries embedded in AGN disks to determine the accretion dynamics and secular evolution of the binary, covering a range of values for the parameters $\lambda, q/h^3, \gamma, M_1/M_2$, and e_b. The flows close to the binary (including the CSDs) are generally found to be more massive with decreasing γ and with increasing q/h^3 and λ; they are also hotter and more turbulent with increasing γ, q/h^3, and λ. The time-averaged accretion rate $\langle\dot{M}_b\rangle$ (in units of $\Sigma_{bg}a_b v_b$) depends on the physical size of the accretor (see above), and monotonically decreases with γ and increases with q/h^3. In general, circular comparable-mass binaries contract if the EOS is far from isothermal, with an orbital decay rate of a few times the mass doubling rate. When the EOS is close to isothermal ($\gamma = 1$), the binary orbit expands (however, retrograde binaries always experience orbital decay; see also Li et al. 2021). Eccentric binaries tend to experience eccentricity damping. Prograde binaries with higher eccentricities or smaller mass ratios tend to have slower orbital decay rates, with some extreme cases exhibiting orbital expansion. Note that some of the quantitative results may be modified by 3D effects when $q/h^3 \lesssim$ a few (Dempsey et al. 2022). The accretion flows are highly variable, and the dominant variability frequency is the apparent binary orbital frequency (in the rotating frame around the central MBH) for circular binaries but gradually shifts to the radial epicyclic frequency as the binary eccentricity increases. These calculations also suggest that the hardening timescales of the binaries are much shorter than their migration timescales in the AGN disk for all reasonable binary and disk parameters. Overall, these studies show that the dynamics of binaries embedded in AGN disks is quite different from that of isolated binaries in their own CBDs. Obviously, current simulations are still idealized, and future works will be needed to assess the effects of additional physics (e.g., magnetic fields, radiation, and accretion feedbacks) on the evolution of BH binaries in AGN disks.

7. SUMMARY AND FUTURE PROSPECTS

Accretion disks have long played a central role in many areas of astronomy, from bright X-ray sources associated with accreting compact objects in the Galaxy to outflows and jets associated with AGNs, to various complex processes and phenomena associated with star and planet formation. When the central accreting object is replaced by a binary, a new set of dynamical behaviors become important, including Lindblad torques and cavity opening, accretion variabilities on different timescales, eccentricity driving and precession of the inner disk, preferential accretion and long-term binary evolution, and, in the case of misaligned accretion, disk warping and breaking, and secular evolution toward alignment or polar alignment, etc. All these dynamical behaviors have direct or indirect observational manifestations.

Because circumbinary accretion involves intrinsically 2D or 3D phenomena, numerical simulations are crucial to unravel its dynamical behaviors and obtain quantitative answers to some of the key questions, with semianalytic theory providing complementary insights. These simulations are challenging (compared to "normal" accretion disk simulations) because of the wide range of spatial scales (from $\gg a_{\rm b}$ for the circumbinary region to $\ll a_{\rm b}$ for the CSDs) and timescales (from $\ll P_{\rm b}$ to $\gg P_{\rm b}$) involved. For example, to determine the secular effect of accretion on the binary evolution, sufficiently long simulations must be carried out in order to average out the highly dynamical flow behaviors. As a result, systematic numerical simulations have so far focused on idealized 2D setups, with simple EOS (usually locally isothermal) and viscosity prescription. Some key findings include the following:

- Circumbinary accretion is highly dynamical, and the accretion variability is dominated by the period of $P_{\rm b}$ or $\sim 5P_{\rm b}$, depending the binary eccentricity and mass ratio.
- The inner region ($\lesssim 10a_{\rm b}$) of the CBD can develop coherent eccentric structure, which may modulate the accretion and affect the physical processes (such as planet migration) taking place in the disk.
- Over long timescales, a binary undergoing accretion evolves toward equal masses between the components.
- Although the gravitational torque between the binary disk and CBD tends to drive binary orbital decay, once the inner disk region is sufficiently relaxed and accretion sets in, the net angular momentum transfer between the binary and the disk depends on the competition between the accretion and gravitational torques. Circumbinary accretion does not necessarily lead to binary orbit decay, as commonly assumed; the secular orbital evolution depends on the binary parameters (such as the mass ratio and eccentricity) and the thermodynamic properties of the accreting gas. In general, the binary orbital decay/expansion rate is on the order of the mass doubling rate, i.e., $\dot{a}_{\rm b}/a_{\rm b} \sim \pm \dot{M}_{\rm b}/M_{\rm b}$.

Much work remains to go beyond these "idealized" simulations in order to systematically evaluate the roles of gas thermodynamics and magnetic fields (which can generate turbulent viscosity and outflows). Note that the above results apply to the regime in which the local disk mass near the binary is much less than $M_{\rm b}$. When this condition is not satisfied, the flow and binary dynamics can be quite different. For example, in the early stages of young binary stars and MBHBs, the local disk/envelope surrounding the binary can be much more massive than the binary, and the disk self-gravity is important—such massive disks can drive rapid binary orbital decay. Eventually, the local disk "thins out," and we are back to the "proper" circumbinary accretion regime that determines the late-stage binary evolution.

On the observational front, the study of accreting protostellar binaries and the detailed characterization of "mature" binary stars (e.g., using *Gaia*) can shed light on the circumbinary accretion process in the aftermath of star formation. Similarly, the observation of accreting MBHBs (e.g.,

through variable light curves) and the future detection of low-frequency GWs from such binaries (by the PTAs and by the space interferometers such as LISA) will help constrain the assembly history of MBHs and the role of circumbinary accretion.

The CBD can often be misaligned with the orbital plane of the central binary, as expected in realistic scenarios of star formation and MBH evolution. Such misaligned accretion gives rise to the following new dynamical features:

- A misaligned disk is warped, and the "degree" of the warp depends on the internal hydrodynamical stresses of the disk (viscosity and bending waves). Under some conditions, a highly warped disk may break up into two or more separate "rings."
- Over long (viscous) timescales, a misaligned disk around a low-eccentricity binary tends to evolve toward alignment driven by viscous dissipation. When the binary eccentricity is significant, the CBD can evolve toward "polar alignment," with the disk plane perpendicular to the binary plane.

Numerical simulations of misaligned disks are challenging because they require capturing the large-scale disk warps while resolving small-scale dissipations. Much remains to be done in the future, e.g., to evaluate the possibility and condition of disk breaking. Observationally, polar-aligned CBDs have already been detected, and future characterization of misaligned disks would help constrain the binary formation/migration process. Will highly misaligned planets be detected in the future?

Binaries embedded in a "big" disk present a special type of circumbinary accretion. The mass supply/accretion onto such a binary depends on the intricate coupling between the small-scale (within the binary) and large-scale flow dynamics. The orbital evolution of the binary depends on several dimensionless parameters as well as the gas thermodynamics. It has been suggested that some merging BH binaries detected by LIGO/Virgo are produced by binaries embedded in AGN disks. Future observations, including more merger events and related EM counterparts, may provide a more definitive answer.

DISCLOSURE STATEMENT

The authors are not aware of any affiliations, memberships, funding, or financial holdings that might be perceived as affecting the objectivity of this review.

ACKNOWLEDGMENTS

The writing of this review has been motivated by several seminars/colloquia that D.L. gave on this topic in the past few years, most recently at the Kavli Institute for Theoretical Physics; the University of California, Berkeley; Caltech; the University of Illinois Urbana-Champaign; Kavli Institute of Astronomy and Astrophysics; Tsung-Dao Lee Institute; and Harvard University. We thank our collaborators, including Xuening Bai, Francois Foucart, Lars Hernquist, Katlin Kratter, Jiaru Li, Rixin Li, Yoram Lithwick, Adam Dempsey, Ryan Miranda, Volker Springel, Haiyang Wang, and J.J. Zanazzi, for their contributions and insights. We also thank Adam Dempsey, Julian Krolik, Gordon Ogilvie, Eliot Quataert and Noam Soker for useful comments on an early version of this article. This work has been supported in part by the National Science Foundation grant AST-17152 and NASA grant 80NSSC19K0444, and by Cornell University.

LITERATURE CITED

Aly H, Dehnen W, Nixon C, King A. 2015. *MNRAS* 449:65–76
Amaro-Seoane P, Audley H, Babak S, et al. 2017. arXiv:1702.00786

Antoniadis J. 2014. *Ap. J. Lett.* 797(2):L24
Antonini F, Perets HB. 2012. *Ap. J.* 757:27
Armstrong DJ, Osborn HP, Brown DJA, et al. 2014. *MNRAS* 444(2):1873–83
Artymowicz P. 1983. *ACTAA* 33:223–41
Artymowicz P, Lubow SH. 1994. *Ap. J.* 421:651–67
Artymowicz P, Lubow SH. 1996. *Ap. J. Lett.* 467:L77–80
Bailey A, Stone JM, Fung J. 2021. *Ap. J.* 915(2):113
Bailey V, Meshkat T, Reiter M, et al. 2014. *Ap. J. Lett.* 780:L4
Bardeen JM, Petterson JA. 1975. *Ap. J. Lett.* 195:L65–67
Bartos I, Kocsis B, Haiman Z, Márka S. 2017. *Ap. J.* 835(2):165
Baruteau C, Cuadra J, Lin DNC. 2011. *Ap. J.* 726:28
Basri G, Johns-Krull CM, Mathieu RD. 1997. *Astron. J.* 114:781–92
Bate MR. 1998. *Ap. J. Lett.* 508:L95–98
Bate MR. 2000. *MNRAS* 314:33–53
Bate MR, Bonnell IA. 1997. *MNRAS* 285:33–48
Bate MR, Bonnell IA, Bromm V. 2002. *MNRAS* 336(3):705–13
Bate MR, Bonnell IA, Bromm V. 2003. *MNRAS* 339(3):577–99
Bate MR, Bonnell IA, Price NM. 1995. *MNRAS* 277(2):362–76
Bate MR, Lodato G, Pringle JE. 2010. *MNRAS* 401(3):1505–13
Begelman MC, Blandford RD, Rees MJ. 1980. *Nature* 287(5780):307–9
Belczynski K, Holz DE, Bulik T, O'Shaughnessy R. 2016. *Nature* 534(7608):512–15
Bennett DP, Rhie SH, Udalski A, et al. 2016. *Astron. J.* 152(5):125
Bertotti B, Carr BJ, Rees MJ. 1983. *MNRAS* 203:945–54
Beuermann K, Hessman FV, Dreizler S, et al. 2010. *Astron. Astrophys.* 521:L60
Bhaskar HG, Li G, Lin DNC. 2022. *Ap. J.* 934(2):141
Bi J, van der Marel N, Dong R, Muto T, Martin RG, et al. 2020. *Ap. J. Lett.* 895:L18
Bogdanović T, Miller MC, Blecha L. 2022. *Liv. Rev. Relativity* 25:3
Boley AC, Mejía AC, Durisen RH, et al. 2006. *Ap. J.* 651:517–34
Bollen D, Kamath D, Van Winckel H, De Marco O, Wardle M. 2021. *MNRAS* 502(1):445–62
Bollen D, Kamath D, Van Winckel H, et al. 2022. *Astron. Astrophys.* 666:A40
Bonnell I, Bastien P. 1992. *Ap. J.* 401:654–66
Bonnell IA, Bate MR. 1994. *MNRAS* 271:999–1004
Bowen DB, Campanelli M, Krolik JH, Mewes V, Noble SC. 2017. *Ap. J.* 838:42
Bowen DB, Mewes V, Campanelli M, et al. 2018. *Ap. J. Lett.* 853:L17
Bowen DB, Mewes V, Noble SC, et al. 2019. *Ap. J.* 879(2):76
Brinch C, Jørgensen JK, Hogerheijde MR, Nelson RP, Gressel O. 2016. *Ap. J. Lett.* 830:L16
Bromley BC, Kenyon SJ. 2015. *Ap. J.* 806:98
Burke-Spolaor S. 2011. *MNRAS* 410(4):2113–22
Burke-Spolaor S, Taylor SR, Charisi M, et al. 2019. *Astron. Astrophys.* 27:5
Capelo HL, Herbst W, Leggett SK, Hamilton CM, Johnson JA. 2012. *Ap. J. Lett.* 757:L18
Carr JS, Mathieu RD, Najita JR. 2001. *Ap. J.* 551:454–60
Chapon D, Mayer L, Teyssier R. 2013. *MNRAS* 429(4):3114–22
Charisi M, Bartos I, Haiman Z, et al. 2016. *MNRAS* 463(2):2145–71
Charisi M, Taylor SR, Runnoe J, Bogdanovic T, Trump JR. 2022. *MNRAS* 510(4):5929–44
Chiang EI, Murray-Clay RA. 2004. *Ap. J.* 607(2):913–20
Coleman GAL, Nelson RP, Triaud AHMJ. 2022. *MNRAS* 513(2):2563–80
Colpi M. 2014. *Space Sci. Rev.* 183(1–4):189–221
Combi L, Armengol FGL, Campanelli M, et al. 2021. *Phys. Rev. D* 104(4):044041
Combi L, Lopez Armengol FG, Campanelli M, et al. 2022. *Ap. J.* 928(2):187
Cossins P, Lodato G, Clarke CJ. 2009. *MNRAS* 393(4):1157–73
Cuadra J, Armitage PJ, Alexander RD, Begelman MC. 2009. *MNRAS* 393(4):1423–32
Czekala I, Andrews SM, Jensen ELN, et al. 2015. *Ap. J.* 806(2):154

Czekala I, Andrews SM, Torres G, et al. 2016. *Ap. J.* 818(2):156
Czekala I, Chiang E, Andrews SM, et al. 2019. *Ap. J.* 883:22
Czekala I, Ribas Á, Cuello N, et al. 2021. *Ap. J.* 912:6
De Rosa A, Vignali C, Bogdanović T, et al. 2019. *New Astron. Rev.* 86:101525
de Val-Borro M, Gahm GF, Stempels HC, Pepliński A. 2011. *MNRAS* 413(4):2679–88
de Val-Borro M, Karovska M, Sasselov D. 2009. *Ap. J.* 700(2):1148–60
Dempsey AM, Lee WK, Lithwick Y. 2020a. *Ap. J.* 891(2):108
Dempsey AM, Li H, Mishra B, Li S. 2022. *Ap. J.* 940(2):155
Dempsey AM, Muñoz D, Lithwick Y. 2020b. *Ap. J. Lett.* 892(2):L29
Dempsey AM, Muñoz DJ, Lithwick Y. 2021. *Ap. J. Lett.* 918(2):L36
Deng H, Ogilvie GI. 2022. *MNRAS* 512(4):6078–92
Deng H, Ogilvie GI, Mayer L. 2021. *MNRAS* 500(3):4248–56
Dermine T, Izzard RG, Jorissen A, Van Winckel H. 2013. *Astron. Astrophys.* 551:A50
Detweiler S. 1979. *Ap. J.* 234:1100–4
Dittmann AJ, Ryan G. 2021. *Ap. J.* 921:71
Dittmann AJ, Ryan G. 2022. *MNRAS* 513(4):6158–76
Doolin S, Blundell KM. 2011. *MNRAS* 418(4):2656–68
D'Orazio DJ, Di Stefano R. 2018. *MNRAS* 474(3):2975–86
D'Orazio DJ, Duffell PC. 2021. *Ap. J. Lett.* 914:L21
D'Orazio DJ, Haiman Z, Duffell P, MacFadyen A, Farris B. 2016. *MNRAS* 459(3):2379–93
D'Orazio DJ, Haiman Z, MacFadyen A. 2013. *MNRAS* 436(4):2997–3020
D'Orazio DJ, Haiman Z, Schiminovich D. 2015. *Nature* 525(7569):351–53
Dotti M, Colpi M, Haardt F, Mayer L. 2007. *MNRAS* 379(3):956–62
Doyle LR, Carter JA, Fabrycky DC, et al. 2011. *Science* 333(6049):1602–6
Duffell PC. 2016. *Ap. J. Suppl.* 226:2
Duffell PC, D'Orazio D, Derdzinski A, et al. 2020. *Ap. J.* 901:25
Duffell PC, MacFadyen AI. 2012. *Ap. J.* 755:7
Dunhill AC, Cuadra J, Dougados C. 2015. *MNRAS* 448(4):3545–54
Dutrey A, Guilloteau S, Simon M. 1994. *Astron. Astrophys.* 286:149–59
Dvorak R, Froeschle C, Froeschle C. 1989. *Astron. Astrophys.* 226:335–42
Edgar R. 2004. *New Astron. Rev.* 48(10):843–59
El-Badry K, Rix HW, Tian H, Duchêne G, Moe M. 2019. *MNRAS* 489(4):5822–57
Escala A, Larson RB, Coppi PS, Mardones D. 2005. *Ap. J.* 630:152–66
Fairbairn CW, Ogilvie GI. 2021. *MNRAS* 508(2):2426–46
Farago F, Laskar J. 2010. *MNRAS* 401(2):1189–98
Farris BD, Duffell P, MacFadyen AI, Haiman Z. 2014. *Ap. J.* 783(2):134
Fielding DB, McKee CF, Socrates A, Cunningham AJ, Klein RI. 2015. *MNRAS* 450(3):3306–18
Foucart F, Lai D. 2013. *Ap. J.* 764:106
Foucart F, Lai D. 2014. *MNRAS* 445(2):1731–44
Franchini A, Lupi A, Sesana A. 2022. *Ap. J. Lett.* 929:L13
Franchini A, Sesana A, Dotti M. 2021. *MNRAS* 507:1458–67
Fung J, Artymowicz P, Wu Y. 2015. *Ap. J.* 811(2):101
Gammie CF, Goodman J, Ogilvie GI. 2000. *MNRAS* 318(4):1005–16
Gaskell CM. 1996. *Ap. J. Lett.* 464:L107–10
Goldreich P, Sari R. 2003. *Ap. J.* 585(2):1024–37
Goldreich P, Tremaine S. 1979. *Ap. J.* 233:857–71
Goldreich P, Tremaine S. 1980. *Ap. J.* 241:425–41
Goodchild S, Ogilvie G. 2006. *MNRAS* 368(3):1123–31
Gould A, Rix HW. 2000. *Ap. J. Lett.* 532:L29–32
Goulding AD, Pardo K, Greene JE, et al. 2019. *Ap. J. Lett.* 879(2):L21
Graham MJ, Djorgovski SG, Stern D, et al. 2015. *Nature* 518(7537):74–76
Gualandris A, Read JI, Dehnen W, Bortolas E. 2017. *MNRAS* 464(2):2301–10

Günther R, Kley W. 2002. *Astron. Astrophys.* 387:550–59
Haehnelt MG. 1994. *MNRAS* 269:199–208
Haiman Z, Kocsis B, Menou K. 2009. *Ap. J.* 700(2):1952–69
Halbwachs JL, Mayor M, Udry S, Arenou F. 2003. *Astron. Astrophys.* 397:159–75
Hanawa T, Ochi Y, Ando K. 2010. *Ap. J.* 708:485–97
Heath RM, Nixon CJ. 2020. *Astron. Astrophys.* 641:A64
Hirose M, Osaki Y. 1990. *Publ. Astron. Soc. Jpn.* 42:135–63
Holman MJ, Wiegert PA. 1999. *Astron. J.* 117:621–28
Hopkins PF. 2015. *MNRAS* 450:53–110
Hopkins PF, Hernquist L, Cox TJ, et al. 2006. *Ap. J. Suppl.* 163:1–49
Hu BX, D'Orazio DJ, Haiman Z, et al. 2020. *MNRAS* 495(4):4061–70
Hwang HC, El-Badry K, Rix HW, et al. 2022. *Ap. J. Lett.* 933(2):L32
Ichikawa T, Kido M, Takaishi D, et al. 2021. *Ap. J.* 919:55
Ireland MJ, Kraus AL. 2008. *Ap. J. Lett.* 678:L59–62
Jensen ELN, Akeson R. 2014. *Nature* 511(7511):567–69
Jensen ELN, Dhital S, Stassun KG, et al. 2007. *Astron. J.* 134:241–51
Jensen ELN, Mathieu RD. 1997. *Astron. J.* 114:301–16
Kanagawa KD, Muto T, Tanaka H, et al. 2016. *Publ. Astron. Soc. Jpn.* 68(3):43
Kashi A, Soker N. 2011. *MNRAS* 417(2):1466–79
Kelley LZ. 2021. *MNRAS* 500(3):4065–77
Kelley LZ, Blecha L, Hernquist L. 2017a. *MNRAS* 464(3):3131–57
Kelley LZ, Blecha L, Hernquist L, Sesana A, Taylor SR. 2017b. *MNRAS* 471(4):4508–26
Kelley LZ, Blecha L, Hernquist L, Sesana A, Taylor SR. 2018. *MNRAS* 477:964–76
Kelley LZ, Haiman Z, Sesana A, Hernquist L. 2019. *MNRAS* 485(2):1579–94
Kennedy GM, Matrà L, Facchini S, et al. 2019. *Nat. Astron.* 3:230–35
Kennedy GM, Wyatt MC, Sibthorpe B, et al. 2012a. *MNRAS* 421(3):2264–76
Kennedy GM, Wyatt MC, Sibthorpe B, et al. 2012b. *MNRAS* 426(3):2115–28
King AR, Pringle JE. 2006. *MNRAS* 373:L90–92
Kley W, Dirksen G. 2006. *Astron. Astrophys.* 447:369–77
Kley W, Haghighipour N. 2014. *Astron. Astrophys.* 564:A72
Kley W, Thun D, Penzlin ABT. 2019. *Astron. Astrophys.* 627:A91
Kluska J, Van Winckel H, Coppée Q, et al. 2022. *Astron. Astrophys.* 658:A36
Kormendy J, Ho LC. 2013. *Annu. Rev. Astron. Astrophys.* 51:511–653
Kostov VB, Orosz JA, Feinstein AD, et al. 2020. *Astron. J.* 159(6):253
Kostov VB, Powell BP, Orosz JA, et al. 2021. *Astron. J.* 162(6):234
Kratter KM, Matzner CD, Krumholz MR. 2008. *Ap. J.* 681:375–90
Kratter KM, Murray-Clay RA, Youdin AN. 2010. *Ap. J.* 710(2):1375–86
Kraus S, Kreplin A, Young AK, et al. 2020. *Science* 369(6508):1233–38
Kremer K, Chatterjee S, Ye CS, Rodriguez CL, Rasio FA. 2019. *Ap. J.* 871:38
Kumar S, Pringle JE. 1985. *MNRAS* 213:435–42
Kuruwita RL, Federrath C, Haugbølle T. 2020. *Astron. Astrophys.* 641:A59
Kuwahara A, Kurokawa H, Ida S. 2019. *Astron. Astrophys.* 623:A179
Lagrange AM, Langlois M, Gratton R, et al. 2016. *Astron. Astrophys.* 586:L8
Lee WK, Dempsey AM, Lithwick Y. 2019a. *Ap. J.* 872(2):184
Lee WK, Dempsey AM, Lithwick Y. 2019b. *Ap. J. Lett.* 882:L11
Li D, Zhou JL, Zhang H. 2014. *MNRAS* 437(4):3832–41
Li G, Holman MJ, Tao M. 2016. *Ap. J.* 831:96
Li J, Dempsey AM, Li H, Lai D, Li S. 2023. *Ap. J. Lett.* 944(2):L42
Li J, Lai D, Rodet L. 2022. *Ap. J.* 934(2):154
Li R, Lai D. 2022. *MNRAS* 517(2):1602–24
Li R, Lai D. 2023. *MNRAS* 522(2):1881–94
Li YP, Dempsey AM, Li H, Li S, Li J. 2022. *Ap. J. Lett.* 928(2):L19

Li YP, Dempsey AM, Li S, Li H, Li J. 2021. *Ap. J.* 911(2):124
LIGO Sci. Collab., Virgo Collab., KAGRA Collab., et al. 2021. arXiv:2111.03606
Lin MK, Papaloizou JCB. 2011. *MNRAS* 415(2):1445–68
Lines S, Leinhardt ZM, Baruteau C, Paardekooper SJ, Carter PJ. 2015. *Astron. Astrophys.* 582:A5
Lipunov VM, Postnov KA, Prokhorov ME. 1997. *Astron. Lett.* 23(4):492–97
Lithwick Y, Wu Y. 2008. arXiv:0802.2951
Liu B, Lai D. 2018. *Ap. J.* 863:68
Liu B, Lai D. 2019. *MNRAS* 483(3):4060–69
Liu B, Lai D. 2021. *MNRAS* 502(2):2049–64
Liu B, Lai D, Wang YH. 2019a. *Ap. J. Lett.* 883:L7
Liu B, Muñoz DJ, Lai D. 2015. *MNRAS* 447:747–64
Liu T, Gezari S, Ayers M, et al. 2019b. *Ap. J.* 884:36
Liu T, Gezari S, Burgett W, et al. 2016. *Ap. J.* 833:6
Lodato G, Price DJ. 2010. *MNRAS* 405(2):1212–26
Lubow SH. 1991a. *Ap. J.* 381:259–67
Lubow SH. 1991b. *Ap. J.* 381:268–77
Lubow SH. 2022. *MNRAS* 516(4):5446–53
Lubow SH, Artymowicz P. 1996. In *Evolutionary Processes in Binary Stars*, *Proc. NATO Adv. Study Inst.*, ed. RAMJ Wijers, MB Davies, CA Tout, Vol. 477, pp. 53–73. Dordrecht: Kluwer Acad. Publ.
Lubow SH, Martin RG. 2018. *MNRAS* 473(3):3733–46
Lubow SH, Ogilvie GI. 2000. *Ap. J.* 538:326–40
Lubow SH, Ogilvie GI, Pringle JE. 2002. *MNRAS* 337(2):706–12
Lucy LB. 2006. *Astron. Astrophys.* 457(2):629–35
Lucy LB, Ricco E. 1979. *Astron. J.* 84:401–12
Lynden-Bell D, Kalnajs AJ. 1972. *MNRAS* 157:1–30
MacFadyen AI, Milosavljević M. 2008. *Ap. J.* 672:83–93
Magorrian J, Tremaine S, Richstone D, et al. 1998. *Astron. J.* 115(6):2285–305
Martin DV, Triaud AHMJ. 2014. *Astron. Astrophys.* 570:A91
Martin DV, Triaud AHMJ, Udry S, et al. 2019. *Astron. Astrophys.* 624:A68
Martin RG, Lubow SH. 2017. *Ap. J. Lett.* 835(2):L28
Martin RG, Lubow SH. 2019. *MNRAS* 490:1332–49
Marzari F, Thébault P, Scholl H. 2008. *Ap. J.* 681(2):1599–608
Masset FS. 2008. *EAS Publ. Ser.* 29:165–244
Masset FS, Morbidelli A, Crida A, Ferreira J. 2006. *Ap. J.* 642:478–87
Mathieu RD, Stassun K, Basri G, et al. 1997. *Astron. J.* 113:1841–54
Matzner CD, Levin Y. 2005. *Ap. J.* 628(2):817–31
Matzner RA, Huq MF, Shoemaker D. 1998. *Phys. Rev. D* 59(2):024015
Maureira MJ, Pineda JE, Segura-Cox DM, et al. 2020. *Ap. J.* 897:59
Mayer L, Kazantzidis S, Madau P, et al. 2007. *Science* 316(5833):1874–77
McKee CF, Ostriker EC. 2007. *Annu. Rev. Astron. Astrophys.* 45:565–687
McKernan B, Ford KES, Bellovary J, et al. 2018. *Ap. J.* 866:66
McKernan B, Ford KES, Kocsis B, Lyra W, Winter LM. 2014. *MNRAS* 441:900–9
McKernan B, Ford KES, Lyra W, Perets HB. 2012. *MNRAS* 425:460–69
Meschiari S. 2012. *Ap. J. Lett.* 761:L7
Middleton H, Chen S, Del Pozzo W, Sesana A, Vecchio A. 2018. *Nat. Commun.* 9:573
Milosavljević M, Merritt D. 2001. *Ap. J.* 563:34–62
Milosavljević M, Merritt D. 2003a. *AIP Conf. Proc.* 686:201
Milosavljević M, Merritt D. 2003b. *Ap. J.* 596:860–78
Milosavljević M, Phinney ES. 2005. *Ap. J. Lett.* 622(2):L93–96
Mingarelli CMF, Lazio TJW, Sesana A, et al. 2017. *Nat. Astron.* 1:886–92
Miranda R, Lai D. 2015. *MNRAS* 452(3):2396–409
Miranda R, Muñoz DJ, Lai D. 2017. *MNRAS* 466:1170–91

Miranda R, Rafikov RR. 2019. *Ap. J. Lett.* 878:L9
Miranda R, Rafikov RR. 2020. *Ap. J.* 892:65
Moe M, Di Stefano R. 2013. *Ap. J.* 778(2):95
Moe M, Di Stefano R. 2017. *Ap. J. Suppl.* 230(2):15
Moody MSL, Shi JM, Stone JM. 2019. *Ap. J.* 875:66
Moriwaki K, Nakagawa Y. 2004. *Ap. J.* 609(2):1065–70
Muñoz DJ, Kratter K, Springel V, Hernquist L. 2014. *MNRAS* 445(4):3475–95
Muñoz DJ, Kratter K, Vogelsberger M, Hernquist L, Springel V. 2015. *MNRAS* 446(2):2010–29
Muñoz DJ, Lai D. 2016. *Ap. J.* 827:43
Muñoz DJ, Lai D, Kratter K, Miranda R. 2020. *Ap. J.* 889(2):114
Muñoz DJ, Lithwick Y. 2020. *Ap. J.* 905(2):106
Muñoz DJ, Miranda R, Lai D. 2019. *Ap. J.* 871:84
Muñoz DJ, Stone NC, Petrovich C, Rasio FA. 2022. arXiv:2204.06002
Murray CD, Dermott SF. 2000. *Solar System Dynamics*. Cambridge, UK: Cambridge Univ. Press
Muzerolle J, Furlan E, Flaherty K, Balog Z, Gutermuth R. 2013. *Nature* 493(7432):378–80
Nealon R, Price DJ, Pinte C. 2020. *MNRAS* 493:L143–47
Nixon C, King A, Price D. 2013. *MNRAS* 434(3):1946–54
Noble SC, Mundim BC, Nakano H, et al. 2012. *Ap. J.* 755:51
Offner SSR, Kratter KM, Matzner CD, Krumholz MR, Klein RI. 2010. *Ap. J.* 725(2):1485–94
Offner SSR, Moe M, Kratter KM, et al. 2022. In *Protostars and Planets VII*, ed. S Inutsuka, Y Aikawa, T Muto, K Tomida, M Tamura. Tucson: Univ. Ariz. Press. In press. **http://ppvii.org/chapter/08/**
Ogilvie GI. 1999. *MNRAS* 304(3):557–78
Ogilvie GI. 2006. *MNRAS* 365(3):977–90
Ogilvie GI, Latter HN. 2013. *MNRAS* 433(3):2403–19
Paardekooper SJ, Leinhardt ZM, Thébault P, Baruteau C. 2012. *Ap. J. Lett.* 754:L16
Paardekooper SJ, Ogilvie GI. 2019. *MNRAS* 483(3):3738–53
Pakmor R, Springel V, Bauer A, et al. 2016. *MNRAS* 455:1134–43
Papaloizou JCB, Lin DNC. 1995. *Ap. J.* 438:841–51
Papaloizou JCB, Nelson RP, Kley W, Masset FS, Artymowicz P. 2007. In *Protostars and Planets V*, ed. B Reipurth, D Jewitt, K Keil, pp. 655–68. Tucson: Univ. Ariz. Press
Papaloizou JCB, Pringle JE. 1983. *MNRAS* 202:1181–94
Pejcha O, Metzger BD, Tomida K. 2016. *MNRAS* 455(4):4351–72
Pelupessy FI, Portegies Zwart S. 2013. *MNRAS* 429:895–902
Penzlin ABT, Kley W, Nelson RP. 2021. *Astron. Astrophys.* 645:A68
Phinney ES. 2001. arXiv:astro–ph/0108028
Phuong NT, Dutrey A, Diep PN, Guilloteau S, Chapillon E, et al. 2020. *Astron. Astrophys.* 635:A12
Pichardo B, Sparke LS, Aguilar LA. 2005. *MNRAS* 359(2):521–30
Pierens A, Nelson RP. 2008. *Astron. Astrophys.* 483(2):633–42
Pierens A, Nelson RP. 2013. *Astron. Astrophys.* 556:A134
Pilat-Lohinger E, Funk B, Dvorak R. 2003. *Astron. Astrophys.* 400:1085–94
Polnarev AG, Rees MJ. 1994. *Astron. Astrophys.* 283:301–12
Poon M, Zanazzi JJ, Zhu W. 2021. *MNRAS* 503(2):1599–614
Portegies Zwart SF, McMillan SLW. 2000. *Ap. J. Lett.* 528:L17–20
Pringle JE. 1981. *Annu. Rev. Astron. Astrophys.* 19:137–62
Pringle JE. 1991. *MNRAS* 248:754–59
Qian SB, Dai ZB, Liao WP, et al. 2009. *Ap. J. Lett.* 706:L96–99
Rafikov RR. 2005. *Ap. J. Lett.* 621:L69–72
Rafikov RR. 2013. *Ap. J. Lett.* 764:L16
Rafikov RR. 2016. *Ap. J.* 830:8
Raghavan D, McAlister HA, Henry TJ, et al. 2010. *Ap. J. Suppl.* 190:1–42
Ragusa E, Alexander R, Calcino J, Hirsh K, Price DJ. 2020. *MNRAS* 499(3):3362–80
Ragusa E, Lodato G, Price DJ. 2016. *MNRAS* 460(2):1243–53

Rajagopal M, Romani RW. 1995. *Ap. J.* 446:543–49
Rodet L, Beust H, Bonnefoy M, et al. 2017. *Astron. Astrophys.* 602:A12
Rodriguez C, Taylor GB, Zavala RT, et al. 2006. *Ap. J.* 646:49–60
Roedig C, Sesana A, Dotti M, et al. 2012. *Astron. Astrophys.* 545:A127
Sandquist EL, Taam RE, Chen X, Bodenheimer P, Burkert A. 1998. *Ap. J.* 500(2):909–22
Sazhin MV. 1978. *Sov. Astron.* 22:36–38
Scheuer PAG, Feiler R. 1996. *MNRAS* 282:291–94
Scholl H, Marzari F, Thébault P. 2007. *MNRAS* 380(3):1119–26
Sesana A, Haardt F, Madau P, Volonteri M. 2005. *Ap. J.* 623:23–30
Sesana A, Vecchio A, Colacino CN. 2008. *MNRAS* 390:192–209
Shannon RM, Ravi V, Lentati LT, et al. 2015. *Science* 349(6255):1522–25
Shi JM, Krolik JH. 2015. *Ap. J.* 807(2):131
Shi JM, Krolik JH, Lubow SH, Hawley JF. 2012. *Ap. J.* 749(2):118
Shu FH, Lubow SH, Anderson L. 1979. *Ap. J.* 229:223–41
Silsbee K, Rafikov RR. 2015. *Ap. J.* 808:58
Silsbee K, Tremaine S. 2017. *Ap. J.* 836:39
Sirko E, Goodman J. 2003. *MNRAS* 341(2):501–8
Siwek M, Weinberger R, Muñoz DJ, Hernquist L. 2022. *MNRAS* 518(4):5059–71
Siwek MS, Kelley LZ, Hernquist L. 2020. *MNRAS* 498:537–47
Smallwood JL, Franchini A, Chen C, et al. 2020. *MNRAS* 494:487–99
Socia QJ, Welsh WF, Orosz JA, et al. 2020. *Astron. J.* 159(3):94
Springel V. 2010. *MNRAS* 401(2):791–851
Stamatellos D, Whitworth AP. 2008. *Astron. Astrophys.* 480(3):879–87
Stone NC, Metzger BD, Haiman Z. 2017. *MNRAS* 464:946–54
Tagawa H, Haiman Z, Kocsis B. 2020. *Ap. J.* 898:25
Takaishi D, Tsukamoto Y, Suto Y. 2020. *MNRAS* 492(4):5641–54
Tang Y, Haiman Z, MacFadyen A. 2018. *MNRAS* 476(2):2249–57
Tang Y, MacFadyen A, Haiman Z. 2017. *MNRAS* 469(4):4258–67
Teyssandier J, Ogilvie GI. 2016. *MNRAS* 458(3):3221–47
Thompson TA, Quataert E, Murray N. 2005. *Ap. J.* 630:167–85
Thorne KS. 1987. In *Three Hundred Years of Gravitation*, ed. SW Hawking, W Israel, pp. 330–458. Cambridge, UK: Cambridge Univ. Press
Thun D, Kley W. 2018. *Astron. Astrophys.* 616:A47
Thun D, Kley W, Picogna G. 2017. *Astron. Astrophys.* 604:A102
Tiede C, Zrake J, MacFadyen A, Haiman Z. 2020. *Ap. J.* 900:43
Tobin JJ, Kratter KM, Persson MV, et al. 2016. *Nature* 538(7626):483–86
Tofflemire BM, Mathieu RD, Ardila DR, et al. 2017a. *Ap. J.* 835:8
Tofflemire BM, Mathieu RD, Herczeg GJ, Akeson RL, Ciardi DR. 2017b. *Ap. J. Lett.* 842(2):L12
Tofflemire BM, Mathieu RD, Johns-Krull CM. 2019. *Astron. J.* 158(6):245
Tokovinin A, Moe M. 2020. *MNRAS* 491(4):5158–71
Tokovinin AA. 2000. *Astron. Astrophys.* 360:997–1002
Tremaine S, Touma J, Namouni F. 2009. *Astron. J.* 137(3):3706–17
Tsukamoto Y, Machida MN. 2013. *MNRAS* 428(2):1321–34
Van Winckel H. 2018. arXiv:1809.00871
Van Winckel H, Lloyd Evans T, Briquet M, et al. 2009. *Astron. Astrophys.* 505(3):1221–32
Vasiliev E, Antonini F, Merritt D. 2015. *Ap. J.* 810:49
Volonteri M, Pfister H, Beckmann RS, et al. 2020. *MNRAS* 498(2):2219–38
Volonteri M, Pfister H, Beckmann R, et al. 2022. *MNRAS* 514:640–56
Wang H, Bai X, Lai D. 2022a. *Ap. J.* 943:175
Wang HY, Bai XN, Lai D, Lin DNC. 2022b. arXiv:2212.07416
Ward WR. 1997. *Icarus* 126(2):261–81
Welsh WF, Orosz JA. 2018. In *Handbook of Exoplanets*, ed. HJ Deeg, JA Belmonte, id. 34. Cham, Switz.: Springer

Whitworth AP, Stamatellos D. 2006. *Astron. Astrophys.* 458(3):817–29
Winn JN, Holman MJ, Johnson JA, Stanek KZ, Garnavich PM. 2004. *Ap. J. Lett.* 603:L45–48
Witt CA, Charisi M, Taylor SR, Burke-Spolaor S. 2022. *Ap. J.* 936:89
Xu W, Stone JM. 2019. *MNRAS* 488(4):5162–84
Youdin AN, Kratter KM, Kenyon SJ. 2012. *Ap. J.* 755:17
Yu Q, Tremaine S. 2002. *MNRAS* 335(4):965–76
Zanazzi JJ, Lai D. 2018b. *MNRAS* 473:603–15
Zanazzi JJ, Lai D. 2018a. *MNRAS* 477(4):5207–19
Zhao B, Li ZY. 2013. *Ap. J.* 763:7
Zhu W, Bernhard K, Dai F, et al. 2022. *Ap. J. Lett.* 933:L21
Zhu Z, Ju W, Stone JM. 2016. *Ap. J.* 832(2):193
Zimmerman RL, Hellings RW. 1980. *Ap. J.* 241:475–85
Zrake J, Tiede C, MacFadyen A, Haiman Z. 2021. *Ap. J. Lett.* 909:L13

Contents

Annual Review of Astronomy and Astrophysics
Volume 61, 2023

Indexes

Errata

An online log of corrections to *Annual Review of Astronomy and Astrophysics* articles may be found at http://www.annualreviews.org/errata/astro